Acknowledgments—We thank Drs. W. Hammerschmidt, H. J. Delecluse, K. Shimotohno, and A. Aronheim for providing the EBV-BAC system, HEK293 cells, expression vectors for CREB and c-Jun, and anti-JDP2 antibodies, respectively. XBP1 cDNA was a kind gift from Dr. K. Mori. We also express our appreciation to T. Gamano for technical assistance.

REFERENCES

1. Speck, S. H., Chatila, T., and Flemington, E. (1997) *Trends Microbiol.* **5,** 399–405
2. Amon, W., and Farrell, P. J. (2005) *Rev. Med. Virol.* **15,** 149–156
3. Tsurumi, T., Fujita, M., and Kudoh, A. (2005) *Rev. Med. Virol.* **15,** 3–15
4. Flemington, E., and Speck, S. H. (1990) *J. Virol.* **64,** 1217–1226
5. Liu, S., Liu, P., Borras, A., Chatila, T., and Speck, S. H. (1997) *EMBO J.* **16,** 143–153
6. Liu, S., Borras, A. M., Liu, P., Suske, G., and Speck, S. H. (1997) *Virology* **228,** 11–18
7. Liu, P., Liu, S., and Speck, S. H. (1998) *J. Virol.* **72,** 8230–8239
8. Ruf, I. K., and Rawlins, D. R. (1995) *J. Virol.* **69,** 7648–7657
9. Flemington, E., and Speck, S. H. (1990) *J. Virol.* **64,** 1227–1232
10. Aronheim, A., Zandi, E., Hennemann, H., Elledge, S. J., and Karin, M. (1997) *Mol. Cell. Biol.* **17,** 3094–3102
11. Ostrovsky, O., Bengal, E., and Aronheim, A. (2002) *J. Biol. Chem.* **277,** 40043–40054
12. Kawaida, R., Ohtsuka, T., Okutsu, J., Takahashi, T., Kadono, Y., Oda, H., Hikita, A., Nakamura, K., Tanaka, S., and Furukawa, H. (2003) *J. Exp. Med.* **197,** 1029–1035
13. Nakade, K., Pan, J., Yoshiki, A., Ugai, H., Kimura, M., Liu, B., Li, H., Obata, Y., Iwama, M., Itohara, S., Murata, T., and Yokoyama, K. K. (2007) *Cell Death Differ.* **14,** 1398–1405
14. Jin, C., Li, H., Murata, T., Sun, K., Horikoshi, M., Chiu, R., and Yokoyama, K. K. (2002) *Mol. Cell. Biol.* **22,** 4815–4826
15. Lerdrup, M., Holmberg, C., Dietrich, N., Shaulian, E., Herdegen, T., Jäättelä, M., and Kallunki, T. (2005) *Biochim. Biophys. Acta* **1745,** 29–37
16. Piu, F., Aronheim, A., Katz, S., and Karin, M. (2001) *Mol. Cell. Biol.* **21,** 3012–3024
17. Heinrich, R., Livne, E., Ben-Izhak, O., and Aronheim, A. (2004) *J. Biol. Chem.* **279,** 5708–5715
18. Blazek, E., Wasmer, S., Kruse, U., Aronheim, A., Aoki, M., and Vogt, P. K. (2003) *Oncogene* **22,** 2151–2159
19. Bitton-Worms, K., Pikarsky, E., and Aronheim, A. (2010) *Mol. Cancer* **9,** 54
20. Nakade, K., Pan, J., Yamasaki, T., Murata, T., Wasylyk, B., and Yokoyama, K. K. (2009) *J. Biol. Chem.* **284,** 10808–10817
21. Rasmussen, M. H., Sørensen, A. B., Morris, D. W., Dutra, J. C., Engelhard, E. K., Wang, C. L., Schmidt, J., and Pedersen, F. S. (2005) *Virology* **337,** 353–364
22. Hwang, H. C., Martins, C. P., Bronkhorst, Y., Randel, E., Berns, A., Fero, M., and Clurman, B. E. (2002) *Proc. Natl. Acad. Sci. U.S.A.* **99,** 11293–11298
23. Jin, C., Ugai, H., Song, J., Murata, T., Nili, F., Sun, K., Horikoshi, M., and Yokoyama, K. K. (2001) *FEBS Lett.* **489,** 34–41
24. Jin, C., Kato, K., Chimura, T., Yamasaki, T., Nakade, K., Murata, T., Li, H., Pan, J., Zhao, M., Sun, K., Chiu, R., Ito, T., Nagata, K., Horikoshi, M., and Yokoyama, K. K. (2006) *Nat. Struct. Mol. Biol.* **13,** 331–338
25. Wardell, S. E., Boonyaratanakornkit, V., Adelman, J. S., Aronheim, A., and Edwards, D. P. (2002) *Mol. Cell. Biol.* **22,** 5451–5466
26. Weidenfeld-Baranboim, K., Bitton-Worms, K., and Aronheim, A. (2008) *Nucleic Acids Res.* **36,** 3608–3619
27. Murata, T., Hotta, N., Toyama, S., Nakayama, S., Chiba, S., Isomura, H., Ohshima, T., Kanda, T., and Tsurumi, T. (2010) *J. Biol. Chem.* **285,** 23925–23935
28. Murata, T., Isomura, H., Yamashita, Y., Toyama, S., Sato, Y., Nakayama, S., Kudoh, A., Iwahori, S., Kanda, T., and Tsurumi, T. (2009) *Virology* **389,** 75–81
29. Murata, T., Sato, Y., Nakayama, S., Kudoh, A., Iwahori, S., Isomura, H., Tajima, M., Hishiki, T., Ohshima, T., Hijikata, M., Shimotohno, K., and Tsurumi, T. (2009) *J. Biol. Chem.* **284,** 8033–8041
30. Ego, T., Tanaka, Y., and Shimotohno, K. (2005) *Oncogene* **24,** 1914–1923
31. Matsumoto, J., Ohshima, T., Isono, O., and Shimotohno, K. (2005) *Oncogene* **24,** 1001–1010
32. Yoshida, H., Matsui, T., Yamamoto, A., Okada, T., and Mori, K. (2001) *Cell* **107,** 881–891
33. Nakayama, S., Murata, T., Yasui, Y., Murayama, K., Isomura, H., Kanda, T., and Tsurumi, T. (2010) *J. Virol.* **84,** 12589–12598
34. Delecluse, H. J., Hilsendegen, T., Pich, D., Zeidler, R., and Hammerschmidt, W. (1998) *Proc. Natl. Acad. Sci. U.S.A.* **95,** 8245–8250
35. Bhende, P. M., Dickerson, S. J., Sun, X., Feng, W. H., and Kenney, S. C. (2007) *J. Virol.* **81,** 7363–7370
36. Feng, W. H., Kraus, R. J., Dickerson, S. J., Lim, H. J., Jones, R. J., Yu, X., Mertz, J. E., and Kenney, S. C. (2007) *J. Virol.* **81,** 10113–10122
37. Zhang, Q., Wang, Y. C., and Montalvo, E. A. (1999) *Virology* **255,** 160–170
38. Yu, X., Wang, Z., and Mertz, J. E. (2007) *PLoS Pathog.* **3,** e194
39. Kraus, R. J., Perrigoue, J. G., and Mertz, J. E. (2003) *J. Virol.* **77,** 199–207
40. Ellis, A. L., Wang, Z., Yu, X., and Mertz, J. E. (2010) *J. Virol.* **84,** 6139–6152
41. Thomas, C., Dankesreiter, A., Wolf, H., and Schwarzmann, F. (2003) *J. Gen. Virol.* **84,** 959–964
42. Montalvo, E. A., Cottam, M., Hill, S., and Wang, Y. J. (1995) *J. Virol.* **69,** 4158–4165

JOURNAL OF VIROLOGY, July 2011, p. 6127–6135 Vol. 85, No. 13
0022-538X/11/$12.00 doi:10.1128/JVI.00258-11

Spatiotemporally Different DNA Repair Systems Participate in Epstein-Barr Virus Genome Maturation▽

Atsuko Sugimoto,[1,2] Teru Kanda,[1] Yoriko Yamashita,[3] Takayuki Murata,[1] Shinichi Saito,[1] Daisuke Kawashima,[1] Hiroki Isomura,[1] Yukihiro Nishiyama,[2] and Tatsuya Tsurumi[1]*

Division of Virology, Aichi Cancer Center Research Institute, Chikusa-ku, Nagoya 464-8681, Japan,[1] and Department of Virology[2] and Department of Pathology and Biological Responses,[3] Nagoya University Graduate School of Medicine, Showa-ku, Nagoya 466-8550, Japan

Received 4 February 2011/Accepted 4 April 2011

Productive replication of Epstein-Barr virus occurs in discrete sites in nuclei, called replication compartments, where viral DNA replication proteins and host homologous recombinational repair (HRR) and mismatch repair (MMR) factors are recruited. Three-dimensional (3D) surface reconstruction imaging clarified the spatial arrangements of these factors within the replication compartments. Subnuclear domains, designated BMRF1 cores, which were highly enriched in viral polymerase processivity factor BMRF1 could be identified inside the replication compartments. Pulse-chase experiments revealed that newly synthesized viral genomes organized around the BMRF1 cores were transferred inward. HRR factors could be demonstrated mainly outside BMRF1 cores, where *de novo* synthesis of viral DNA was ongoing, whereas MMR factors were found predominantly inside. These results imply that *de novo* synthesis of viral DNA is coupled with HRR outside the cores, followed by MMR inside cores for quality control of replicated viral genomes. Thus, our approach unveiled a viral genome manufacturing plant.

Epstein-Barr virus (EBV), a human lymphotropic herpesvirus with a linear double-stranded DNA 172 kb in length (2), infects resting B lymphocytes, inducing their continuous proliferation without production of virus particles, this being termed latent infection. Productive infection, which occurs spontaneously or can be induced artificially, is characterized by expression of lytic genes, leading to virus production. The EBV genome is amplified 100- to 1,000-fold by viral replication machinery composed of BALF5 DNA polymerase, BMRF1 polymerase processivity factor, BALF2 single-stranded-DNA (ssDNA) binding protein, and BBLF4-BSLF1-BBLF2/3 helicase-primase complex in discrete sites in nuclei, which are called replication compartments (9, 13). With progression of productive replication, the replication compartments become enlarged and fuse to form large globular structures that eventually fill the nucleus in late stages (9).

We have previously reported the architecture of the EBV replication compartments (9). The BZLF1 *oriLyt* binding proteins show a fine, diffuse pattern of distribution throughout the nuclei at immediate-early stages of induction and then become associated with the replicating EBV genome in the replication compartments during lytic infection. The BMRF1 proteins show a homogenous, not dot-like, distribution in the replication compartments, coinciding with the synthesized viral DNA. In contrast, the BALF5 Pol catalytic protein, the BALF2 single-stranded-DNA binding protein, and the BBLF2/3 protein, a component of the helicase-primase complex, were colocalized as distinct dots distributed within replication compartments, representing viral replication factories.

The BMRF1 protein is a major phosphoprotein abundantly expressed during EBV productive infection (7, 26), associating with the BALF5 polymerase catalytic subunit with one-to-one stoichiometry to enhance its polymerase processivity (41). Judging from immunostaining data, together with the finding that almost all expressed BMRF1 proteins bind to viral genome DNA, the factor has been assumed not only to act as a polymerase processivity factor but also to protect the viral genome after synthesis. In addition, it can transcriptionally activate the BHLF1 promoter (48) and enhance BZLF1-mediated transcription of the BALF2 promoter (33).

It has been suggested that DNA replication is coupled with DNA recombination to generate large branched head-to-tail concatemers of replication intermediates during herpesvirus genome replication (4, 44, 49). We previously showed that homologous recombinational repair (HRR) factors such as replication protein A (RPA), Rad51, Rad52, and the Mre11/Rad50/Nbs1 (MRN) complex are recruited and loaded onto the newly synthesized viral genome in replication compartments (23). HRR is an accurate repair process known to be mediated by the MRN complex, RPA, members of the RAD52 epistasis group of gene products such as Rad51, Rad52, and Rad54, and phosphorylated BRCA1 and BRCA2 (5, 24). Knockdown of RPA32 and Rad51 by RNA interference significantly prevents viral DNA synthesis (23), indicating an HRR involvement in viral DNA synthesis.

We have also previously demonstrated that proliferating cell nuclear antigen (PCNA), the PCNA loader complex (RF-C), and a series of mismatch repair (MMR) proteins such as MSH2, MSH6, MLH1, and PMS2 can be assembled to Epstein-Barr virus replication compartments (10). MMR works primarily to correct mutations by removing base-base and

* Corresponding author. Mailing address: Division of Virology, Aichi Cancer Center Research Institute, Kanokoden, Chikusa-ku, Nagoya 464-8681, Japan. Phone and fax: 81-52-764-2979. E-mail: ttsurumi@aichi-cc.jp.

▽ Published ahead of print on 13 April 2011.

small insertion-deletion mismatches that arise during DNA replication, and it is mediated by MSH heterodimers (MSH2-MSH3 and MSH2-MSH6) and MLH heterodimers (MLH1-PMS2 and MLH1-MLH3) (18, 20). PCNA, which was originally characterized as a DNA sliding clamp for replicative DNA polymerases, interacts with MSH2-MSH6 or MSH2-MSH3 complexes, searching for mispairs on newly replicated DNA (8, 14, 19). RF-C recruits PCNA (the clamp) and loads it onto DNA in the presence of ATP (clamp loading), with this being required for MMR (47).

In other herpesviruses such as herpes simplex virus type 1 (HSV-1) and human cytomegalovirus (HCMV), viral replication compartments are also formed in the infected nuclei during the productive replication, and HRR factors, including the MRN complex and Rad51, are reported to be recruited to the replication compartments (27, 29, 36, 37, 46). Furthermore, Taylor and Knipe reported that the HSV-1-encoded single-stranded-DNA binding protein ICP8 interacts either directly or indirectly with HRR and MMR factors (37). Also, HSV-1 alkaline exonuclease UL12 has recently been shown to interact specifically with the MRN complex (3).

Here we examined the spatial arrangements of viral DNA replication factors and cellular HRR and MMR factors in the replication compartments by means of confocal laser scanning microscopy and three-dimensional (3D) surface reconstruction imaging. BMRF1-rich subnuclear domains, designated BMRF1 cores, could be identified inside the replication compartments. As a result, each replication compartment was partitioned into two subdomains, outside and inside the BMRF1 core. We here present data demonstrating that viral DNA replication and viral genome maturation are assigned to outside and inside subdomains, respectively.

MATERIALS AND METHODS

Cell culture. Tet-BZLF1/B95-8 cells were maintained in RPMI 1640 medium supplemented with 1 μg/ml puromycin, 250 μg/ml hygromycin B, and 10% tetracycline-free fetal calf serum (Clontech) at 37°C in a humidified 5% CO_2 atmosphere. To induce lytic EBV replication, the tetracycline derivative doxycycline was added to the culture medium at a final concentration of 4 μg/ml. When blocking lytic replication, phosphonoacetic acid (PAA), a herpesvirus DNA polymerase-specific inhibitor, was added to the culture medium at a final concentration of 400 μg/ml.

Antibodies. Anti-BALF2 and anti-BMRF1 rabbit polyclonal antibodies were as previously prepared (10, 40, 42). Anti-BALF5 protein-specific rabbit antibodies (43) were affinity purified with BALF5 protein coupled-Sepharose 4B as described previously (15). An anti-EBV EA-D-p52/50 (BMRF1 gene product) protein-specific mouse monoclonal antibody, clone name R3, was purchased from Chemicon Inc. 5-Chloro-2′-deoxyuridine (CldU)-labeled DNAs were detected with anti-5-bromo-2′-deoxyuridine (anti-BrdU) rat monoclonal antibody clone BU1/75 (ICR1), purchased from Abcam. The anti-BrdU antibody clone BU1/75 (ICR1) does not cross-react with 5-iodo-2′-deoxyuridine (IdU). Anti-pRPA32 S4/S8, -BRCA1 S1524, and -Mre11 rabbit polyclonal antibodies were purchased from Abcam and anti-Rad52 antibodies from Cell Signaling. Anti-PCNA mouse monoclonal and rabbit polyclonal antibodies were purchased from Transduction Laboratories and Abcam, respectively, and anti-MSH2, -MSH3, and -MSH6 monoclonal antibodies were obtained from Transduction Laboratories and BD Biosciences. The secondary goat anti-rabbit, anti-rat, and anti-mouse IgG antibodies conjugated with Alexa 488 or 594, a Zenon mouse IgG labeling kit (Alexa 594), and a Zenon rabbit IgG labeling kit (Alexa 594) were obtained from Molecular Probes.

Immunofluorescence analysis. All staining procedures except for extraction and incubation with primary antibodies were carried out at room temperature. For immunofluorescence experiments, cells were washed with ice-cold phosphate-buffered saline (PBS) and extracted with 0.5% Triton X-100–mCSK buffer [10 mM piperazine-*N*,*N*′-bis(2-ethanesulfonic acid) (PIPES) (pH 6.8), 300 mM sucrose, 1 mM $MgCl_2$, 1 mM EGTA, 1 mM dithiothreitol, 1 mM phenylmethylsulfonyl fluoride, 0.5% Triton X-100) on ice for 10 min. Multiple protease inhibitors (Sigma; 25 μl/ml), 200 μM Na_3VO_4, and 20 mM NaF were also added to the buffer. Cells were fixed with 70% ethanol for 24 h at −20°C, washed with PBS containing 0.1% normal goat serum and 0.01% Tween 20, permeabilized with 0.5% Triton X-100 in PBS for 15 min, blocked for 1 h in 10% normal goat serum in PBS, and then incubated overnight with the primary antibodies diluted in PBS containing 0.1% normal goat serum and 0.01% Tween 20. The samples were then incubated for 1 h with secondary goat anti-rabbit, anti-rat, and anti-mouse IgG antibodies conjugated with Alexa Fluor 488 or 594. For MSH2, MSH3, and MSH6 staining, anti-MSH2, -MSH3, and -MSH6 antibodies were directly labeled with a Zenon tricolor mouse IgG1 labeling kit purchased from Molecular Probes. Also, for BALF2, BRCA1 S1524, and Rad52 staining, anti-BALF2, -BRCA1 S1524, and -Rad52 antibodies were directly labeled with a Zenon tricolor rabbit IgG1 labeling kit purchased from Molecular Probes. Cells were incubated with Alexa Flour 594-labeled anti-MSH2, -MSH3, -MSH6, -BALF2, -BRCA1 S1524, and -Rad52 antibodies for 45 min at room temperature and washed three times with PBS, followed by a second fixation with 4% paraformaldehyde solution in phosphate buffer for 15 min at room temperature. All the primary antibodies were employed at a 1:100 dilution, and the secondary antibodies were employed at a 1:500 dilution. All washes after antibody incubation were performed with PBS containing 0.1% normal goat serum and 0.01% Tween 20. The slides were mounted in ProLong Gold antifade reagent with 4′,6′-diamidino-2-phenylindole (DAPI) (Molecular Probes) and analyzed by fluorescence confocal microscopy. Laser scanning confocal fluorescence microscopic images were captured and processed using an LSM510 Meta microscope (Carl Zeiss MicroImaging, Inc.) with a plan-Apochromat 100×/1.4-numerical-aperture oil immersion objective.

Pulse-chase experiments. For CldU pulse-labeling, newly synthesized DNA was labeled by incubating lytic replication-induced Tet-BZLF1/B95-8 cells with 10 μM CldU added directly to the incubation medium for 10 min at 24 h postinduction. For the pulse-chase experiments, the cells were pulse-labeled with 10 μM CldU for 10 min at 24 h postinduction, and the CldU-containing medium was removed and replaced with new medium containing IdU to inhibit CldU incorporation to newly synthesized DNA. Cells were chased for 1 h prior to harvesting. Cells were washed with ice-cold PBS and extracted with 0.5% Triton X-100–mCSK buffer on ice for 10 min. Multiple protease inhibitors (Sigma; 25 μl/ml), 200 μM Na_3VO_4, and 20 mM NaF were also added to the buffer. Cells were then fixed with 70% ethanol for 24 h at −20°C and treated for 60 min with 2 N HCl containing 0.5% Triton X-100 to expose the incorporated CldU residues before blocking. The cells were washed twice with PBS and neutralized with 0.1 M sodium tetraborate, pH 9.0, for 5 min prior to immunofluorescence.

Fluorescence in situ hybridization. EBV bacterial artificial chromosome (BAC) DNA was labeled with digoxigenin (DIG) nick translation mix (Sigma) and used as a probe. First, cells were fixed in 4% paraformaldehyde and 70% ethanol. After digestion with RNase, cells were treated with 50% formamide in 2× SSC (1× SSC is 0.15 M NaCl plus 0.015 M sodium citrate), air dried, and immediately covered with a probe mixture containing 60% formamide in 2× SSC containing probe DNA (4 ng/μl), 12% dextran sulfate, and sheared salmon DNA (0.1 μg/μl). Probes and cells were simultaneously heated at 85°C for 5 min and incubated overnight at 37°C. After hybridization, specimens were washed at 45°C with 50% formamide in 2× SSC (three times for 3 min each), at 45°C with 2× SSC (three times for 3 min each), and at 65°C with 0.1× SSC for 10 min. After washing, specimens were blocked for 1 h in 5% milk in 4× SCC containing 1% bovine serum albumin (BSA) and then stained with anti-DIG sheep monoclonal antibodies in 4× SSC containing 1% BSA at 37°C for 30 min. After staining, specimens were washed at room temperature with 4× SSC, 0.1% Triton X-100 in 4× SSC, 4× SSC, and PN buffer (0.5 M Na_2HPO_4, 0.5 M NaH_2PO_4, 0.5% NP-40) (three times for 3 min each). Finally, cells were stained with anti-BMRF1 mouse monoclonal antibodies, mounted in ProLong Gold antifade reagent with DAPI (Molecular Probes), and analyzed by fluorescence confocal microscopy. Images were captured and processed using an LSM510 Meta microscope (Carl Zeiss MicroImaging, Inc.) with a plan-Apochromat 100×/1.4-numerical-aperture oil immersion objective.

3D reconstruction with confocal laser scanning microscopy. Images observed with a confocal laser scanning microscope (Carl Zeiss MicroImaging, Inc.) were computerized to automatically make 50 to 100 serial optical sections at intervals of around 0.26 μm. The 3D reconstruction was performed with Imaris software (Carl Zeiss MicroImaging, Inc.). Image files created by the LSM510 Meta microscope were opened with Imaris, and a 3D surface model was created based on the appropriate intensity threshold.

RESULTS

BMRF1-rich structures (cores) are observed in viral replication compartments. We previously described a B95-8 derivative cell line in which we can trigger onset of viral lytic replication via tetracycline-inducible expression of viral immediate-early protein BZLF1 (Tet-BZLF1/B95-8 cells) (22). In this study, we utilized Tet-BZLF1/B95-8 cells to examine more details of replication compartments during viral productive replication. The lytic replication-induced Tet-BZLF1/B95-8 cells were harvested and extracted with 0.5% Triton X-100–mCSK buffer. It should be noted that the treatment extracts soluble viral or cellular proteins, permitting investigation of DNA-bound fractions of viral and cellular proteins. We tested for specificity of the secondary antibodies and for reliability of discrimination with the fluorescence microscopy filters. When cells were stained singly for either antigen with inappropriate combinations of first and second antibodies, no fluorescence was observed. Also, no immunofluorescence was observed with an alternate filter. We have previously defined EBV replication compartments as BMRF1- or BALF2-staining sites where viral DNA genomes are colocalized as judged by immunofluorescence and fluorescence *in situ* hybridization (FISH) analysis (9). A representative image of a viral replication compartment is illustrated in Fig. 1A, visualized by means of indirect immunofluorescence analyses. As shown in a merged image, BALF2 protein dots were distributed not only inside but also outside BMRF1-stained subnuclear domains. A correlative immunofluorescence microscopy and electron microscopic imaging (FM-EM) study found that BMRF1 proteins were localized within an electron-lucent region in the nuclear interior, in contrast with electron-dense chromatin regions (data not shown). At higher magnification, the area corresponding to the replication compartment contained diffuse noncondensed fibers and granules but lacked any specific structures.

In an independent experiment, the localizations of viral genome DNA and BMRF1 protein were simultaneously examined by means of combinational FISH and immunofluorescence. As shown in a representative image (Fig. 1B), the majority of viral genome DNA was localized inside BMRF1-localized regions. To support FISH analysis, we performed pulse-labeling analysis combined with immunofluorescence staining. The labeling reagent CldU, a nucleotide analog like BrdU, was added to the culture medium at 24 h postinduction and left for 10 min so that newly synthesized viral DNAs were labeled with incorporated CldU. As shown in Fig. 1C, CldU staining coincided with BMRF1- and BALF2-localized regions. In the presence of PAA, a herpesvirus DNA polymerase-specific inhibitor, CldU and BMRF1 signals were not observed (Fig. 1C). In the presence of the inhibitor, viral replication compartments are not formed and the expressed BMRF1 proteins are solubilized by the detergent treatment, while BALF2 proteins are distributed throughout nuclei as distinct spots (9). Overall, these results indicate that viral genome DNA is synthesized in the replication compartments, confirming the previous observations (9).

Spatial localization of viral replication proteins within replication compartments. Confocal images are frequently presented as brightest point projections, but this format is not appropriate for demonstrating the spatial distribution of objects. To establish spatial relationships among viral replication proteins within replication compartments, 3D surface reconstruction imaging was employed. We used a 3D visualization and volume modeling software program, Imaris, to create images. We first examined the spatial distribution of BMRF1 relative to viral ssDNA binding protein BALF2 and viral DNA polymerase BALF5. Our previous work demonstrated colocalization of BALF5 with BALF2 as distinct spots within replication compartments, with the two proteins most likely cooperatively working at viral replication forks (9). As illustrated in a representative 3D image (Fig. 2A), each mass of BMRF1 protein appeared to be surrounded by BALF2 protein. We named the BMRF1-rich structures "BMRF1 cores." It should be noted that BALF2 protein also localized inside the BMRF1 core, as observed in 2D images (Fig. 2A). Similarly, as shown in another representative 3D surface reconstruction image (Fig. 2B), each BMRF1 core was surrounded by BALF5 DNA polymerase, although BALF5 was also localized inside the BMRF1 core as shown in the 2D image (Fig. 2B). On the other hands, the BALF5 and BALF2 proteins colocalized well both outside and inside the BMRF1 core (Fig. 2). From the 3D

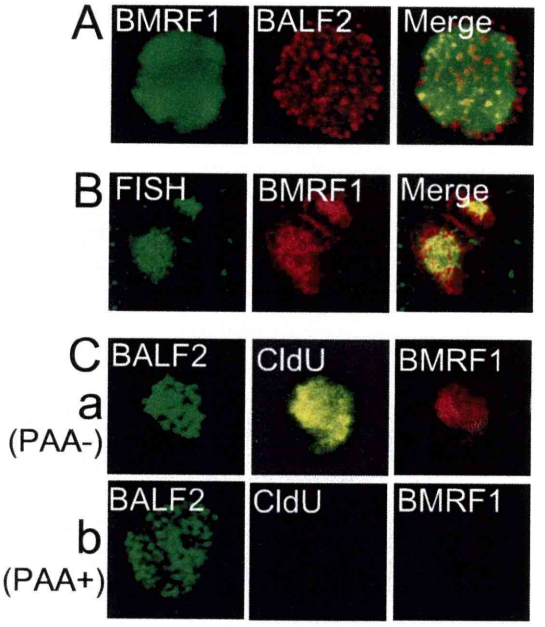

FIG. 1. The majority of viral genome DNA is localized inside BMRF1-rich structures. (A) Lytic replication-induced Tet-BZLF1/B95-8 cells were fixed, stained with anti-BMRF1 (green) and anti-BALF2 (red) antibodies, and observed by laser scanning confocal microscopy to locate viral replication compartments. The right panel is a merged image. (B) Lytic replication-induced Tet-BZLF1/B95-8 cells were fixed in 4% paraformaldehyde and 70% ethanol. After digestion with RNase, they were treated with 50% formamide, air dried, and immediately hybridized with a mixture containing the EBV BAC DNA probe labeled with DIG nick translation mix. Specimens were stained with fluorescein isothiocyanate (FITC)-conjugated anti-DIG sheep (green) and anti-BMRF1 mouse (red) monoclonal antibodies. The right panel is a merged image. (C) Newly synthesized DNAs were labeled by incubation with 10 μM CldU added directly to the culture medium of lytic replication-induced Tet-BZLF1/B95-8 cells for 10 min at 24 h postinduction in the presence (b) or absence (a) of PAA (400 μg/ml). Specimens were stained with anti-BALF2 (green), anti-CldU (yellow), and anti-BMRF1 (red) antibodies.

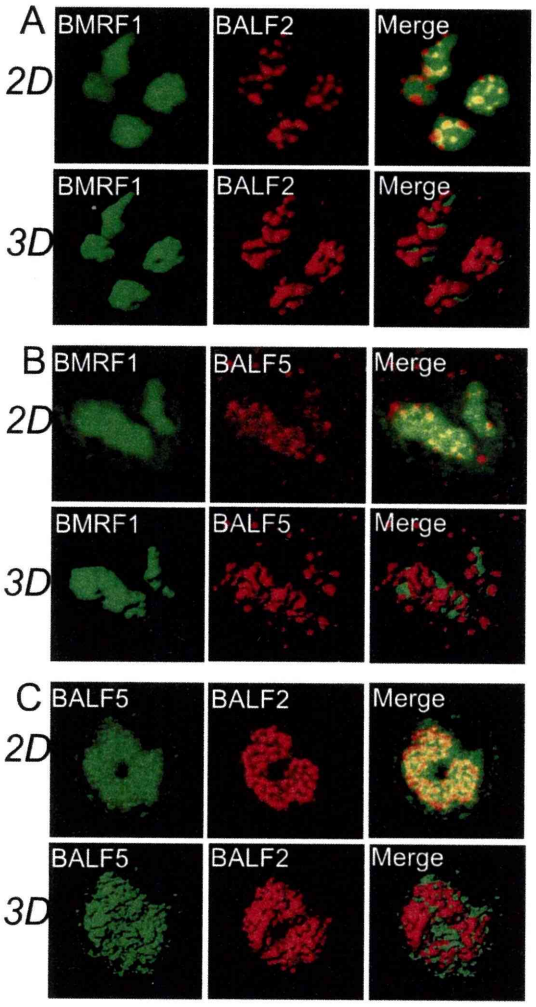

FIG. 2. 3D surface reconstruction imaging of viral replication compartments. (A) Laser scanning confocal images of BMRF1 and BALF2 proteins. Lytic replication-induced Tet-BZLF1/B95-8 cells were treated with 0.5% mCSK buffer, fixed with 70% ethanol, and stained with anti-BMRF1 (green) and anti-BALF2 (red) antibodies. The 2D images show brightest-point projections of 60 images collected at 0.26-μm steps in the *z* axis. The same data are displayed as 3D topographical reconstructions of BMRF1 and BALF2 proteins (left and middle panels, respectively). The right panel shows a 3D surface reconstruction image of both proteins showing the BMRF1 core covered by BALF2 proteins. (B) Laser scanning confocal images of BMRF1 (green) and BALF5 (red) proteins. The 2D images show brightest-point projections of 60 images collected at 0.26-μm steps in the *z* axis. The same data are displayed as 3D topographical reconstructions of BMRF1 and BALF5 proteins (left and middle panels, respectively). The right panel shows a 3D surface reconstruction image of both proteins showing the BMRF1 core covered by BALF5 Pol proteins. (C) Laser scanning confocal images of BALF5 (green) and BALF2 (red) proteins. The 2D images show brightest-point projections of 60 images collected at 0.26-μm steps in the *z* axis. The same data are displayed as 3D topographical reconstructions of BALF5 and BALF2 proteins (left and middle panels, respectively). The right panel shows a 3D surface reconstruction image of both proteins, showing that the BALF5 Pol proteins and BALF2 proteins are mingled.

surface reconstruction image it appeared that both proteins are mingled on their surfaces (Fig. 2C).

Viral DNA genomes newly synthesized outside the BMRF1 core move to the inside. We have previously demonstrated that the sites stained with anti-BMRF1 protein-specific antibodies coincided with the foci of 1-h-pulse-labeled viral DNA as judged by 5-bromodeoxyuridine (BrdU) incorporation and FISH analyses on confocal immunofluorescence analyses and that the BrdU-pulse-labeled DNA moved out of nucleus with time, clarifying that BrdU-labeled DNAs at 24 h postinduction are mostly viral and not cellular DNAs (10).

Our observation that the BMRF1 core was surrounded by a BALF2 ssDNA binding protein and the BALF5 DNA polymerase protein, whereas the majority of viral genomes were inside the core, let us hypothesize that viral DNAs are synthesized outside cores and then transported inside. This hypothesis fits well with the idea that BMRF1, a viral polymerase processivity factor, also protects newly synthesized viral genomes during lytic replication. To test the hypothesis, we performed pulse-chase labeling experiments to monitor the location of newly synthesized viral DNAs. The labeling reagent CldU, a nucleotide analog like BrdU, was added to cells at 24 h postinduction and left for 10 min so that newly synthesized viral DNAs were labeled with incorporated CldU. As shown in a representative image (Fig. 3A), pulse-labeled newly synthesized viral DNAs were localized mainly outside the BMRF1 core, although some existed inside. In contrast, when 1 h of chasing was included after CldU pulse-labeling, all of the labeled viral DNAs were localized inside the BMRF1 core (Fig. 3B). From the 3D surface reconstruction image it appeared that the BALF2 protein and pulse-labeled DNA were mingled (Fig. 3A, bottom panels). These results correspond well with the idea that BMRF1 protein assembles on newly synthesized DNAs to form the cores, and the cores progressively enlarge during the course of productive infection.

HRR proteins are recruited to outside and inside BMRF1 cores. We have previously reported that homologous recombinational repair (HRR) factors such as replication protein A (RPA), Rad51, Rad52, and the Mre11/Nbs1/Rad50 (MRN) complex are recruited and loaded onto the newly synthesized viral genome in replication compartments (23). Therefore, we determined the spatial localization of the HRR factors within these compartments. As shown in a representative image (Fig. 4A), Mre11, a component of the MRN complex, covered and also existed inside the BMRF1 cores. It is noteworthy that the spatial localization of Mre11 (Fig. 4A) resembles that of newly synthesized viral DNAs (Fig. 3A, pulse-labeling without chasing). Similarly, BRCA1, Rad52, and phosphorylated RPA32 at Ser-4/-8 covered the cores (Fig. 4B, C, and D), again resembling the localization of newly synthesized viral DNAs (Fig. 3A). Figure 4D shows relative localizations of BMRF1, BALF2, and phosphorylated RPA (pRPA) within the replication compartment of the same cell. BALF2 and pRPA were colocalized and surrounded the BMRF1 core. This observation corresponds well with our previous demonstration that knockdown of RPA32 and Rad51 by RNA interference significantly prevented viral DNA synthesis (23) and supports the idea that HRR somehow contributes to coordinated viral DNA replication.

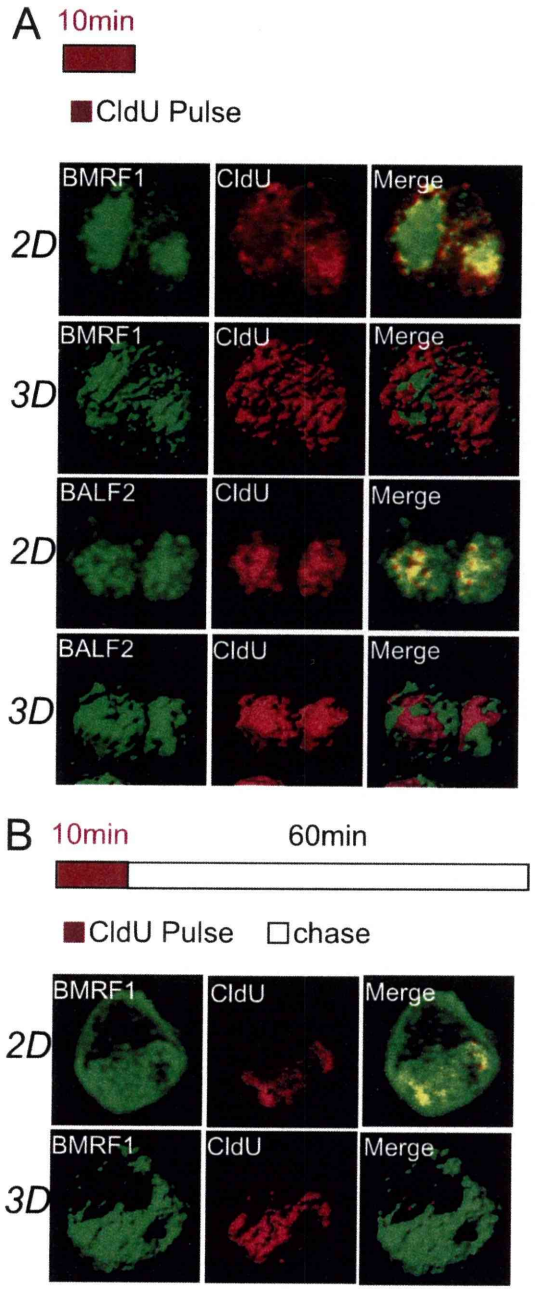

FIG. 3. Newly synthesized viral DNA genomes localized outside the BMRF1 core move to the inside. Pulse-chase labeling experiments were performed with Tet-BZLF1/B95-8 cells at 24 h after induction. Outlines of the experimental protocol are given at the tops of panels A and B. (A) Tet-BZLF1/B95-8 cells were pulse-labeled with CldU for 10 min at 24 h postinduction. (B) The pulse-labeled cells were washed, and then chased for 1 h (B). For the 2D images, cells were treated with 0.5% mCSK buffer and stained with anti-BMRF1 or -BALF2 (green) and anti-CldU (red) antibodies. These images show brightest-point projections of 60 images collected at 0.26-μm steps in the *z* axis. The same data are displayed as 3D topographical reconstructions of the BMRF1 or BALF2 protein and CldU-labeled viral DNA (left and middle panels, respectively). The right panels show 3D surface reconstruction images.

MMR proteins are recruited and loaded inside BMRF1 cores. Next, the spatial localization of mismatch repair (MMR) proteins was determined. As shown in a representative image, the majority of PCNA was localized inside the BMRF1 cores, while some appeared on their surfaces (Fig. 5A). This is in contrast to the localization of HRR factors and MRN complexes (Fig. 4). Regarding the localization of MSH2, MSH3, and MSH6, unlike PCNA, they were almost completely localized inside the BMRF1 cores (Fig. 5B, C, and D). Such a difference in localization implies that MMR factors are last to be loaded onto viral DNAs, whereas the BMRF1 protein and PCNA are first loaded on newly synthesized viral DNA, resulting in enlargement of the BMRF1 core. Because MSH3 and MSH6 interact with PCNA, such loading might trigger transfer of a series of host MMR proteins to sites of viral DNA maturation. Taken together, the results indicate that MMR of the viral DNA genome might occur after BMRF1 proteins bind to a viral DNA and contribute to a mature intact viral genome.

DISCUSSION

Previous cross-sectional studies of EBV replication compartments by confocal laser microscopy demonstrated EBV replication proteins to be localized at viral replication compartments, also revealing variation in staining pattern between individual proteins (9). Here, the BMRF1 protein, which is multifunctional, showed a homogenous, not dot-like, distribution. This is evidence of BMRF1-rich structures (BMRF1 cores) existing within viral replication compartments. Three-dimensional surface reconstruction imaging revealed that replication compartments are partitioned into two subdomains, inside and outside the BMRF1 core. This approach further revealed factories for viral genome synthesis and maturation mediated by HRR and MMR host factors. The BALF5 DNA polymerase and BALF2 ssDNA binding protein were almost colocalized outside the cores. Since both proteins are thought to form an item of the viral elongation machinery acting at replication forks on the replicating EBV genome, they would position at sites of viral genome synthesis. Pulse-chase experiments indicated that viral DNA genomes were synthesized mainly outside BMRF1 cores, where HRR factors were localized, with subsequent movement into the cores. On the other hand, MMR proteins were recruited to viral DNAs exclusively inside, indicating that loading of MMR proteins onto viral DNA is likely to occur at the step of viral genome maturation. These observations let us propose a new model of viral DNA synthesis and maturation as follows. First, viral DNA genomes are synthesized by viral replication machinery, which is coupled with homologous recombination with the help of host HRR factors. Next, BMRF1 proteins bound to the newly synthesized viral DNA are assembled to form cores. During the progression of viral replication, the size of the core increases. Inside, MMR factors are loaded through PCNA to repair and mature newly synthesized viral DNA. The observed sequential loading of HRR factors and MMR proteins on newly synthesized viral DNA implies that spatially and temporarily different repair mechanisms are working during EBV genome maturation.

From our recent resolution of the crystal structure of C-terminally truncated BMRF1 protein (32), the molecular struc-

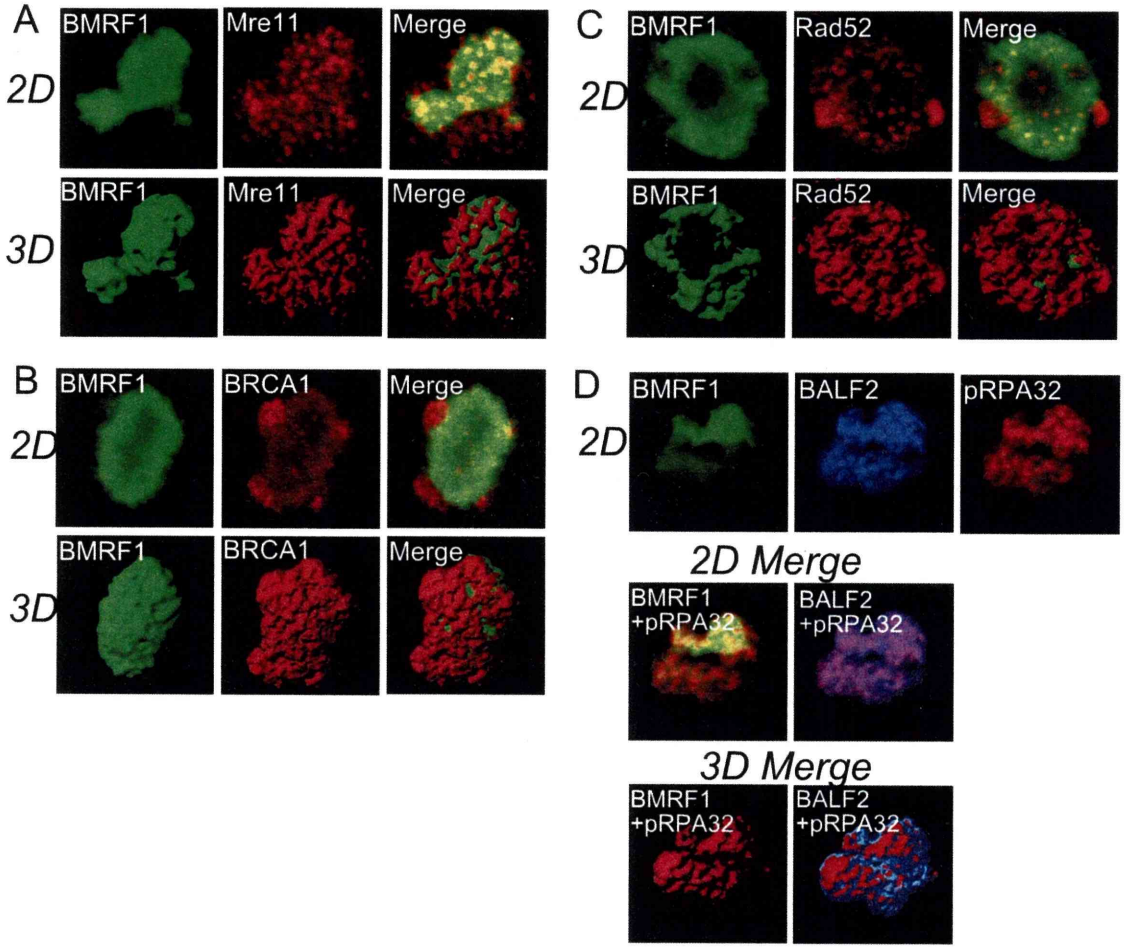

FIG. 4. Homologous recombinational repair proteins are located both outside and inside BMRF1 cores. (A to C) Lytic replication-induced Tet-BZLF1/B95-8 cells were treated with mCSK buffer, fixed with 70% ethanol, and stained with combinations of the indicated antibodies as follows: (A) anti-BMRF1 (green) and anti-Mre11 (red) antibodies; (B) anti-BMRF1 (green) and anti-BRCA1 ser-1524 (red) antibodies; (C) anti-BMRF1 (green) and anti-Rad52 (red) antibodies. The 2D images show brightest-point projections of 60 images collected at 0.26-μm steps in the *z* axis. The same data are displayed as 3D topographical reconstructions of each protein (left and middle panels, respectively). The right panels shows 3D surface reconstruction images of both proteins indicated, showing the BMRF1 core covered by HRR proteins. (D) The cells were stained with anti-BMRF1 (green), anti-BALF2 (blue), and anti-phosphorylated RPA32 Ser-4/Ser-8 (red) antibodies. Top panels, 2D images showing a brightest-point projection of 60 images collected at 0.26-μm steps in the *z* axis. Middle panels, each combination of the merged image of the top panels. Bottom panels, each combination of merged 3D surface reconstruction images.

ture shares structural similarity with other processivity factors, such as HSV-1 UL42, HCMV UL44, and human proliferating cell nuclear antigen (PCNA). Although the crystal structure of BMRF1 indicates an interesting tetramer ring formation, electrophoresis and sedimentation assay suggested that the main component of EBV BMRF1 in solution is a head-to-head dimer. Tail-to-tail association of the dimers forms the ring structure. Replication of a recombinant virus with a point mutation at C206E of BMRF1 (which is expected to impair tail-to-tail contact) is severely restricted (34), although the mutant protein possesses the same *in vitro* biochemical activities as the wild type (32), indicating that its tetrameric ring formation might be essential for EBV replication. PCNA proteins adopt a ring-shaped trimer conformation with the head-to-tail contacts, forming a central channel to accommodate the template DNA (6). The BMRF1 ring-shaped structure (30, 32) is almost twice as large as the previously reported PCNA ring structure. In contrast, HSV-1 UL42 stably exists as a monomer (35), whereas HCMV UL44 forms a head-to-head-contacting C-shaped dimer in the crystal structure (1). The BMRF1 dimer formation overlaps the UL44 dimer. Substitutions of positively charged residues on the concave surface of the BMRF1 C-shaped dimer reduce DNA binding affinity. Furthermore, an amino acid mutation disrupting the dimer formation, C95E, results in no DNA binding (32). Another study of dimerized processivity factor HCMV UL44 also indicates that DNA binding affinity is related to dimer formation (1). Thus, the basic concave surface is very important for DNA binding by the dimerized proteins BMRF1 and UL44. UL44 is consequently thought to bind to DNA like PCNA, which surrounds DNA by ring formation (21). The BMRF1 protein is abundantly expressed in the lytic infected cells and is distributed homogenously, not in a dot-like pattern, within the replication compartments. We speculate that the tetrameric ring form of

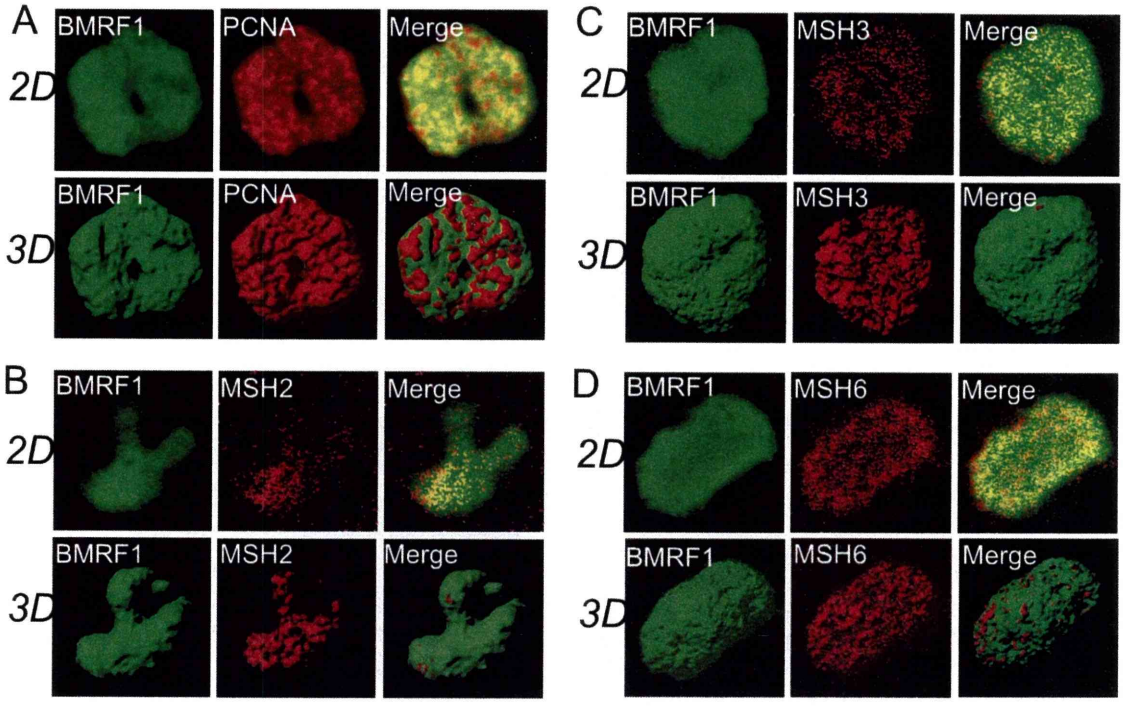

FIG. 5. Mismatch repair proteins such as PCNA, MSH2, MSH3, and MSH6 localize inside BMRF1 cores. Lytic replication-induced Tet-BZLF1/B95-8 cells were treated with mCSK buffer, fixed with 70% ethanol, and stained with combinations of antibodies as follows: (A) anti-BMRF1 (green) and anti-PCNA (red) antibodies; (B) anti-BMRF1 (green) and anti-MSH2 (red) antibodies; (C) anti-BMRF1 (green) and anti-MSH3 (red) antibodies; (D) anti-BMRF1 (green) and anti-MSH6 (red) antibodies. The 2D images show brightest-point projections of 60 images collected at 0.26-μm steps in the z axis. The same data are displayed as a 3D topographical reconstructions of each protein (left and middle panels, respectively). The right panels show 3D surface reconstructions image of both proteins indicated, showing MMR proteins located inside the BMRF1 core.

BMRF1 might be involved in formation of the BMRF1 cores within the replication compartments to protect the synthesized viral DNA by occupying the surfaces of the DNA molecules.

In general, processivity factors are associated with their cognate DNA polymerases on the template during DNA replication. These proteins are also known as "sliding clamps," including PCNA, which interacts with DNA polymerase δ or ε. However, the herpesvirus polymerase processivity factors display different molecular assemblies to cognate viral DNA polymerase. The HSV-1 UL42 form a heterodimer with the UL30 DNA polymerase (35). Mutational analyses of BMRF1 revealed that the monomer form of EBV BMRF1 can function as polymerase processivity factor *in vitro* (32), suggesting that BMRF1 interacts with BALF5 DNA polymerase to form a heterodimer like UL42. Thus, the BMRF1 protein adopts different subunit architecture during the replication process.

HRR is a repair system for double-strand breaks (DSBs), essential for cellular survival in eukaryotes, which relies on several proteins, including Rad-51, -52, and -54, the Mre11/Rad50/Nbs1 (MRN) complex, RPA, and BRCA1/2 (5, 28). First, the MRN complex searches DSBs and generates 3′ ssDNA by removing the 5′ ends of the DSB regions, followed by phosphorylated RPA binding to 3′ ssDNA strands. Rad52, BRCA1, and BRCA2 replace RPA with Rad51. Both Rad51 and Rad52 bind specifically to the terminal region of tailed duplex DNA, the substrate thought to initiate recombination by promoting homologous pairing and strand transfer reactions *in vivo* (12, 16, 38). HRR is also required to repair replication-associated DNA lesions and replication fork stalling or collapse (31, 39). In eukaryotic cells, HRR also occurs coupled with replication at replication forks to ensure proper replication and prevent genomic instability (11). Considering these results and our present study, the host HRR system might be used, being necessary for efficient viral replication coupled with viral genome replication.

It has recently been reported that the HSV-1 alkaline exonuclease UL12 and the single-stranded-DNA binding protein ICP8 interact with each other, are recruited to replication compartments, and together mediate strand exchange *in vitro*, suggesting a role as a two-component recombinase reminiscent of the lambda Red α/β recombination system (3). Further, RPA, Mre11, Rad50, Nbs1, and Rad51 are recruited to HSV-1 replication compartments as in the case of EBV (46). These viral and cellular proteins might together be involved in homologous recombinational repair of herpesvirus genome DNA maturation. However, unlike in the case of EBV (23), there is no induction of hyperphosphorylation of RPA upon productive HSV-1 infection. Instead, endogenous hyperphosphorylated RPA is sequestered away from replication compartments into discrete nuclear foci (VICE domains) that are enriched for cellular components involved in protein folding and degradation (45). Since those authors never observed either induction of RPA hyperphosphorylation or recruitment of phosphorylated RPA to HSV-1 replication compartments, they

concluded that these signaling molecules are excluded from sites that contain viral DNA. Although the discrepancy remains unclear, hyperphosphorylated RPA32, Rad51, Rad52, and MRN complex were recruited to the EBV replication compartments and interacted with EBV genomic DNA (23). HRR represents an error-free subpathway of damage tolerance, allowing replicational bypass of lesions through a template switch. The EBV genome is amplified to several hundred copies during lytic infection, and further, the small interfering RNA (siRNA) depletion of Rad51 or RPA32 reduces new viral DNA synthesis (23). We propose that HRR occurs during EBV lytic genome replication with the aid of host cellular HRR factors and that the HRR factors might help not only to increase the fidelity of viral replication but also to facilitate viral genome replication.

On the other hand, MMR contributes to recognize and repair DNA mismatches that are generated during chromatin DNA replication in eukaryotic cells (20), correcting 99% of such lesions. Because MMR reduces the number of replication-associated errors, defects in MMR increase the spontaneous mutation rate. The MMR machinery works as a postreplication repair near a replication fork. The first step of MMR is that MSH2-MSH6 or MSH2-MSH3 searches for and recognizes a mismatch region through interaction with the β-clamp accessory protein PCNA (14, 18). A MLH1-PMS2 complex is then recruited, and the mismatch region is removed by endonuclease activity of MLH1-PMS2 and exonuclease (Exo1) (17, 25). Thus, this MMR machinery works as a postreplication repair near a replication fork. Our present data show that some MMR proteins contribute to EBV genome maturation after replication. High-copy replication with high fidelity might require the host MMR machinery to repair produced viral genomes.

ACKNOWLEDGMENTS

We thank Ayumi Kudoh (Salk Institute) and Tohru Daikoku (Toyama University) for discussions and Keizo Tomonaga, Yusuke Matsumoto, and Hiroko Omori (Osaka University) and Y. Tanaka (Nagoya University) for technical suggestions.

This work was supported by grants-in-aid for scientific research from the Ministry of Education, Science, Sports, Culture and Technology of Japan (no. 20390137 and 21022055 to T.T.) and partly by the Uehara Memorial Research Fund (to T.T.).

REFERENCES

1. **Appleton, B. A., A. Loregian, D. J. Filman, D. M. Coen, and J. M. Hogle.** 2004. The cytomegalovirus DNA polymerase subunit UL44 forms a C clamp-shaped dimer. Mol. Cell **15**:233–244.
2. **Baer, R., et al.** 1984. DNA sequence and expression of the B95-8 Epstein-Barr virus genome. Nature **310**:207–211.
3. **Balasubramanian, N., P. Bai, G. Buchek, G. Korza, and S. K. Weller.** 2010. Physical interaction between the herpes simplex virus type 1 exonuclease, UL12, and the DNA double-strand break-sensing MRN complex. J. Virol. **84**:12504–12514.
4. **Bataille, D., and A. Epstein.** 1994. Herpes simplex virus replicative concatemers contain L components in inverted orientation. Virology **203**:384–388.
5. **Benson, F. E., P. Baumann, and S. C. West.** 1998. Synergistic actions of Rad51 and Rad52 in recombination and DNA repair. Nature **391**:401–404.
6. **Bruck, I., and M. O'Donnell.** 2001. The ring-type polymerase sliding clamp family. Genome Biol. **2**:REVIEWS3001.
7. **Cho, M. S., G. Milman, and S. D. Hayward.** 1985. A second Epstein-Barr virus early antigen gene in BamHI fragment M encodes a 48- to 50-kilodalton nuclear protein. J. Virol. **56**:860–866.
8. **Clark, A. B., F. Valle, K. Drotschmann, R. K. Gary, and T. A. Kunkel.** 2000. Functional interaction of proliferating cell nuclear antigen with MSH2-MSH6 and MSH2-MSH3 complexes. J. Biol. Chem. **275**:36498–36501.
9. **Daikoku, T., et al.** 2005. Architecture of replication compartments formed during Epstein-Barr virus lytic replication. J. Virol. **79**:3409–3418.
10. **Daikoku, T., et al.** 2006. Postreplicative mismatch repair factors are recruited to Epstein-Barr virus replication compartments. J. Biol. Chem. **281**:11422–11430.
11. **Delacote, F., and B. S. Lopez.** 2008. Importance of the cell cycle phase for the choice of the appropriate DSB repair pathway, for genome stability maintenance: the trans-S double-strand break repair model. Cell Cycle **7**:33–38.
12. **Errico, A., and V. Costanzo.** 2010. Differences in the DNA replication of unicellular eukaryotes and metazoans: known unknowns. EMBO Rep. **11**: 270–278.
13. **Fixman, E. D., G. S. Hayward, and S. D. Hayward.** 1995. Replication of Epstein-Barr virus oriLyt: lack of a dedicated virally encoded origin-binding protein and dependence on Zta in cotransfection assays. J. Virol. **69**:2998–3006.
14. **Flores-Rozas, H., D. Clark, and R. D. Kolodner.** 2000. Proliferating cell nuclear antigen and Msh2p-Msh6p interact to form an active mispair recognition complex. Nat. Genet. **26**:375–378.
15. **Fujita, N., et al.** 1999. Purification, characterization, and cDNA structure of isoamylase from developing endosperm of rice. Planta **208**:283–293.
16. **Gottipati, P., and T. Helleday.** 2009. Transcription-associated recombination in eukaryotes: link between transcription, replication and recombination. Mutagenesis **24**:203–210.
17. **Hoeijmakers, J. H.** 2001. Genome maintenance mechanisms for preventing cancer. Nature **411**:366–374.
18. **Jiricny, J.** 2000. Mediating mismatch repair. Nat. Genet. **24**:6–8.
19. **Kleczkowska, H. E., G. Marra, T. Lettieri, and J. Jiricny.** 2001. hMSH3 and hMSH6 interact with PCNA and colocalize with it to replication foci. Genes Dev. **15**:724–736.
20. **Kolodner, R. D., and G. T. Marsischky.** 1999. Eukaryotic DNA mismatch repair. Curr. Opin. Genet. Dev. **9**:89–96.
21. **Komazin-Meredith, G., et al.** 2008. The human cytomegalovirus UL44 C clamp wraps around DNA. Structure **16**:1214–1225.
22. **Kudoh, A., et al.** 2003. Reactivation of lytic replication from B cells latently infected with Epstein-Barr virus occurs with high S-phase cyclin-dependent kinase activity while inhibiting cellular DNA replication. J. Virol. **77**:851–861.
23. **Kudoh, A., et al.** 2009. Homologous recombinational repair factors are recruited and loaded onto the viral DNA genome in Epstein-Barr virus replication compartments. J. Virol. **83**:6641–6651.
24. **Kuzminov, A.** 2001. DNA replication meets genetic exchange: chromosomal damage and its repair by homologous recombination. Proc. Natl. Acad. Sci. U. S. A. **98**:8461–8468.
25. **Li, G. M.** 2008. Mechanisms and functions of DNA mismatch repair. Cell Res. **18**:85–98.
26. **Li, J. S., et al.** 1987. Association of Epstein-Barr virus early antigen diffuse component and virus-specified DNA polymerase activity. J. Virol. **61**:2947–2949.
27. **Lilley, C. E., C. T. Carson, A. R. Muotri, F. H. Gage, and M. D. Weitzman.** 2005. DNA repair proteins affect the lifecycle of herpes simplex virus 1. Proc. Natl. Acad. Sci. U. S. A. **102**:5844–5849.
28. **Lundin, C., et al.** 2002. Different roles for nonhomologous end joining and homologous recombination following replication arrest in mammalian cells. Mol. Cell. Biol. **22**:5869–5878.
29. **Luo, M. H., K. Rosenke, K. Czornak, and E. A. Fortunato.** 2007. Human cytomegalovirus disrupts both ataxia telangiectasia mutated protein (ATM)- and ATM-Rad3-related kinase-mediated DNA damage responses during lytic infection. J. Virol. **81**:1934–1950.
30. **Makhov, A. M., D. Subramanian, E. Holley-Guthrie, S. C. Kenney, and J. D. Griffith.** 2004. The Epstein-Barr virus polymerase accessory factor BMRF1 adopts a ring-shaped structure as visualized by electron microscopy. J. Biol. Chem. **279**:40358–40361.
31. **Michel, B., et al.** 2001. Rescue of arrested replication forks by homologous recombination. Proc. Natl. Acad. Sci. U. S. A. **98**:8181–8188.
32. **Murayama, K., et al.** 2009. Crystal structure of Epstein-Barr virus DNA polymerase processivity factor BMRF1. J. Biol. Chem. **284**:35896–35905.
33. **Nakayama, S., et al.** 2009. Epstein-Barr virus polymerase processivity factor enhances BALF2 promoter transcription as a coactivator for the BZLF1 immediate-early protein. J. Biol. Chem. **284**:21557–21568.
34. **Nakayama, S., et al.** 2010. Tetrameric ring formation of Epstein-Barr virus polymerase processivity factor is crucial for viral replication. J. Virol. **84**: 12589–12598.
35. **Randell, J. C., and D. M. Coen.** 2004. The herpes simplex virus processivity factor, UL42, binds DNA as a monomer. J. Mol. Biol. **335**:409–413.
36. **Shirata, N., et al.** 2005. Activation of ataxia telangiectasia-mutated DNA damage checkpoint signal transduction elicited by herpes simplex virus infection. J. Biol. Chem. **280**:30336–30341.
37. **Taylor, T. J., and D. M. Knipe.** 2004. Proteomics of herpes simplex virus replication compartments: association of cellular DNA replication, repair, recombination, and chromatin remodeling proteins with ICP8. J. Virol. **78**: 5856–5866.
38. **Thompson, L. H., and J. M. Hinz.** 2009. Cellular and molecular consequences of defective Fanconi anemia proteins in replication-coupled DNA repair: mechanistic insights. Mutat. Res. **668**:54–72.

39. **Toueille, M., and U. Hubscher.** 2004. Regulation of the DNA replication fork: a way to fight genomic instability. Chromosoma **113**:113–125.
40. **Tsurumi, T.** 1993. Purification and characterization of the DNA-binding activity of the Epstein-Barr virus DNA polymerase accessory protein BMRF1 gene products, as expressed in insect cells by using the baculovirus system. J. Virol. **67**:1681–1687.
41. **Tsurumi, T., T. Daikoku, R. Kurachi, and Y. Nishiyama.** 1993. Functional interaction between Epstein-Barr virus DNA polymerase catalytic subunit and its accessory subunit in vitro. J. Virol. **67**:7648–7653.
42. **Tsurumi, T., et al.** 1998. Overexpression, purification and helix-destabilizing properties of Epstein-Barr virus ssDNA-binding protein. J. Gen. Virol. **79**: 1257–1264.
43. **Tsurumi, T., et al.** 1993. Functional expression and characterization of the Epstein-Barr virus DNA polymerase catalytic subunit. J. Virol. **67**:4651–4658.
44. **Weber, P. C., M. D. Challberg, N. J. Nelson, M. Levine, and J. C. Glorioso.** 1988. Inversion events in the HSV-1 genome are directly mediated by the viral DNA replication machinery and lack sequence specificity. Cell **54**:369–381.
45. **Wilkinson, D. E., and S. K. Weller.** 2006. Herpes simplex virus type I disrupts the ATR-dependent DNA-damage response during lytic infection. J. Cell Sci. **119**:2695–2703.
46. **Wilkinson, D. E., and S. K. Weller.** 2004. Recruitment of cellular recombination and repair proteins to sites of herpes simplex virus type 1 DNA replication is dependent on the composition of viral proteins within prereplicative sites and correlates with the induction of the DNA damage response. J. Virol. **78**:4783–4796.
47. **Xie, Y., C. Counter, and E. Alani.** 1999. Characterization of the repeat-tract instability and mutator phenotypes conferred by a Tn3 insertion in RFC1, the large subunit of the yeast clamp loader. Genetics **151**:499–509.
48. **Zhang, Q., et al.** 1996. Functional and physical interactions between the Epstein-Barr virus (EBV) proteins BZLF1 and BMRF1: effects on EBV transcription and lytic replication. J. Virol. **70**:5131–5142.
49. **Zhang, X., S. Efstathiou, and A. Simmons.** 1994. Identification of novel herpes simplex virus replicative intermediates by field inversion gel electrophoresis: implications for viral DNA amplification strategies. Virology **202**: 530–539.

Journal of Clinical Virology 50 (2011) 244–246

Contents lists available at ScienceDirect

Journal of Clinical Virology

journal homepage: www.elsevier.com/locate/jcv

Short communication

Kinetics of Epstein-Barr virus load and virus-specific CD8+ T cells in acute infectious mononucleosis

Yo Hoshino[a], Kazuo Nishikawa[b], Yoshinori Ito[a], Kiyotaka Kuzushima[c], Hiroshi Kimura[d,*]

[a] Department of Pediatrics, Nagoya University Graduate School of Medicine, Japan
[b] Department of Pediatrics, Nagoya Ekisaikai Hospital, Japan
[c] Division of Immunology, Aichi Cancer Center Research Institute, Nagoya, Japan
[d] Department of Virology, Nagoya University Graduate School of Medicine, 65 Tsurumai-Cho, Showa-Ku, Nagoya 466-8550, Japan

ARTICLE INFO

Article history:
Received 20 October 2010
Received in revised form
24 November 2010
Accepted 25 November 2010

Keywords:
Epstein-Barr virus
Infectious mononucleosis
CTL
Viral load
EBV-specific CD8+ T cells

ABSTRACT

Background: During the convalescent phase of acute infectious mononucleosis (AIM), Epstein-Barr virus (EBV) load shrinks rapidly in association with a rapid decline in the number of EBV-specific CD8+ T cells. The actual contribution of EBV-specific CD8+ T cells in reducing EBV load, however, is not known.
Objectives: To clarify the impact of EBV-specific CD8+ T cells on the contraction of EBV load in AIM, we estimated half-lives of both EBV load and EBV-specific CD8+ T cells.
Study design: Blood was serially taken from five pediatric patients with AIM during the convalescent period, including the very early phase, and both EBV load and EBV-specific CD8+ T cell numbers were assayed.
Results: EBV load declined rapidly (half-life 1.5 d) during the first 2 weeks after onset of symptoms. This half-life was seven-fold shorter than that reported for CD27+ memory B cells. Subsequently, the EBV load declined much more slowly, with a half-life of 38.7 d. EBV-specific CD8+ T cell numbers also declined concomitantly with the decrease in EBV load. The half-life of EBV-specific CD8+ T cells during first 2 weeks was 2.9 d. The number of EBV-specific CD8+ T cells and the rate of change of viral load correlated significantly ($R^2 \geq 0.8$; $p \leq 0.02$).
Conclusions: The short half-life of EBV load, together with the strong correlation between the number of EBV-specific CD8+ T cells and the rate of change of viral load indicates an active role for EBV-specific CD8+ T cells in elimination of EBV in AIM.

1. Background

Epstein-Barr virus (EBV) is a ubiquitous viral pathogen that causes acute infectious mononucleosis (AIM) and various malignant diseases, such as Burkitt's lymphoma, nasal NK/T lymphoma, nasopharyngeal carcinoma, and post-transplant lymphoproliferative disorders, in both immunocompromised and immunocompetent hosts.[1] EBV-specific CD8+ T cells play important roles in the control of EBV in these diseases.[2] During the convalescent phase of AIM, the EBV load shrinks rapidly in association with a rapid decline in the number of EBV-specific CD8+ T cells, itself caused by activation-induced cell death.[3] However, the extent to which EBV-specific CD8+ T cells contribute to the decline in EBV load in peripheral blood mononuclear cells remains unknown.

2. Objectives

To clarify the impact of EBV-specific CD8+ T cells on the decline in EBV load, we estimated the half-lives of EBV load and EBV-specific CD8+ T cells during the convalescent period of AIM and also evaluated the correlation between them.

3. Study design

Blood samples were serially obtained from five pediatric patients with AIM after written informed consent had been obtained from their parents. AIM was diagnosed by clinical findings and serological examinations, as previously described.[4] Their ages ranged from 5 to 14 years (median, 9 years). The first samples were obtained within the first week of onset of AIM symptoms. Peripheral blood mononuclear cells were separated, frozen, and stored until required. EBV load in peripheral blood mononuclear cells was measured by real-time PCR and expressed as copies/microgram DNA.[4,5] EBV-specific CD8+ T cells were enumerated by intracellular interferon-γ assay against autologous lymphoblastoid cell lines by

Abbreviations: EBV, Epstein-Barr virus; AIM, acute infectious mononucleosis.

* Corresponding author. Tel.: +81 52 744 2207; fax: +81 52 744 2452.
E-mail address: hkimura@med.nagoya-u.ac.jp (H. Kimura).

1386-6532/$ – see front matter © 2010 Elsevier B.V. All rights reserved.
doi:10.1016/j.jcv.2010.11.017

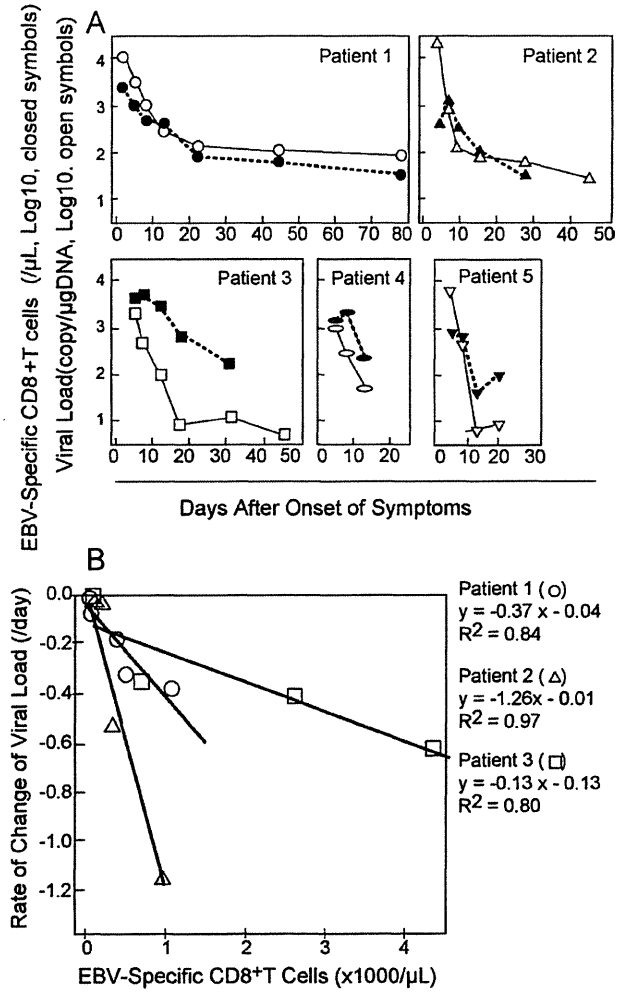

Fig. 1. Kinetics of Epstein-Barr virus (EBV) load and EBV-specific CD8⁺ T cells in patients with acute infectious mononucleosis. (A) EBV vial load was measured by real-time PCR (open symbols connected with solid lines), and EBV-specific CD8⁺ T cell counts by intracellular interferon-γ assay against autologous lymphoblastoid cell lines and flow cytometry (closed symbols connected with broken lines). (B) Correlation between EBV-specific CD8⁺ T cell counts and rate of change in EBV load was estimated by linear regression analysis. Approximations of the rate of change were calculated from three data points. Using v_1, v_2, and v_3, which are the natural logarithms of viral loads at t_1, t_2, and t_3, respectively, the following equation was used to calculate the rate of change of viral load for a unit of viral load at $t=t_2$: $dv/dt_{(t=t2)} = (x_2-x_1)(t_3-t_2)/(t_2-t_1)(t_3-t_1)+(x_3-x_2)(t_2-t_1)/(t_3-t_2)/(t_3-t_1)$. Solid lines indicate linear regression curves for patients 1, 2, and 3, from whom sufficient data points were obtained.

flow cytometry.[3,6]

4. Results

First, we analyzed the kinetics of EBV load and number of EBV-specific CD8⁺ T cells. EBV load was highest at the time of first sampling (2–6 d after onset) in all patients and decreased thereafter (Fig. 1A). Peak viral loads were $10^{4.1}$, $10^{4.3}$, $10^{3.3}$, $10^{3.0}$, and $10^{3.8}$ per μg DNA in patients 1, 2, 3, 4, and 5, respectively. EBV viral loads declined rapidly during the first 1–2 weeks after onset and more slowly thereafter (Fig. 1A). The mean estimated half-life of EBV load during the early convalescent period (~2 weeks after onset) was 1.5 ± 0.2 d (Table 1); this is seven-fold shorter than that reported for CD27⁺ memory B cells (11.1 d).[7] EBV infection in the peripheral blood of AIM patients is restricted to CD27⁺ memory B cells.[8] The mean estimated half-life of EBV load after the 2 weeks was 38.7 ± 15.0. In contrast, number of EBV-specific CD8⁺ T cells increased slightly in three of the five patients and then declined (Fig. 1A). In the remaining patients, the number of EBV-specific CD8⁺ T cells peaked at the time of their first visit ($10^{3.5}$ and $10^{2.9}$ per μL blood in patients 1 and 5, respectively). Number of EBV-specific CD8⁺ T cells declined almost parallel with viral load (half-life 2.9 ± 0.4 d) during the early convalescent period (Table 1).

Table 1
Half-lives of Epstein-Barr virus (EBV) load and EBV-specific CD8⁺ T cells in patients with acute infectious mononucleosis.

Patient	Half-life of EBV load (days)		Half-life of EBV-specific CD8⁺ T cells in acute phase (days) (within 2 weeks of onset)
	Acute phase (within 2 weeks of onset)	Convalescent phase (after 2 weeks of onset)	
1	2.2	22.6	3.8
2	1.5	24.9	2.9
3	1.6	68.7	3.8
4	1.6	n.a.	2.5
5	0.7	n.a.	1.6
Mean ± SE	1.5 ± 0.2	38.7 ± 15.0	2.9 ± 0.4

The shorter half-life of EBV load compared with normal memory B cells suggests the presence of a mechanism that actively removes EBV from blood, such as cytotoxic immune effecter cells. We hypothesized that EBV-specific CD8⁺ T cells play an important role in clearing EBV from blood. EBV load may decrease at a rate proportional to the number of EBV-specific CD8⁺ T cells. To prove this hypothesis, we transformed the time-series of EBV load data into rate of change and examined the correlation between the number of EBV-specific CD8⁺ T cells and the rate of change in viral load. Because multiple data points were necessary for regression analysis, three of the five patients (1, 2, and 3) were analyzed. As shown in Fig. 1B, the analysis revealed a significant positive linear correlation between the rate of change in viral load and the number of EBV-specific CD8⁺ T cells ($R^2 \geq 0.8$, $p \leq 0.02$).

5. Discussion

To clarify the impact of EBV-specific CD8⁺ T cells on the decline in EBV load, we estimated the half-lives of both EBV load and EBV-specific CD8⁺ T cells during the very early phase of the convalescent period of AIM using intervals as short as 2 d. We also evaluated the correlation between the EBV load and the number of EBV-specific CD8⁺ T cells. Our data indicate that during the very early period of AIM, the half-life of EBV load is shorter than that of normal memory B cells and that the rate of change in EBV load was correlated with the number of EBV-specific CD8⁺ T cells in a linear manner. These results suggest that EBV-specific CD8⁺ T cells actively contribute to the decline in EBV load.

Recently, Hadinoto *et al.* reported that linear exponential decay of latent EBV load with a half-life of 7.5 ± 3.7 d was found in patients with AIM during the 30–50 d after the first clinic visit.[9] Due to its similarity to the reported half-life of memory B cells (11.1 d),[7] the authors proposed a model of exponential decay of EBV-infected cells by simple homeostasis of memory B cells, suggesting a passive role for cell-mediated immunity. Hadinoto's paper did not specify the interval between the onset of symptoms and the first clinic visit, and the intervals between assays seemed to be around 1 week. It is possible that EBV-specific CD8⁺ T cells play an important role in the control of EBV load during an earlier stage of AIM. In the very early phase of AIM, EBV infects naïve B cells that express full sets of latent EBV genes.[2] These naïve B cells are either eliminated by EBV-specific CTL or differentiate into memory B cells. In the second phase, the EBV-infected memory B cells express only

restricted kinds of EBV genes,[2] which may help with evasion from EBV-specific CD8+ cells. In the present study, we obtained 2–3 samples per week from the very early period of acute-phase AIM. Thus, the more frequent samples taken at an earlier stage of disease may be the reason for the disagreement in EBV load half-life. In fact, if samples are taken only once per week, a half-life shorter than 3 days will not be detected in two weeks or less.

During the acute phase of AIM, viral loads decreased, even in blood taken only 2 d after symptom onset. Interestingly, we observed a transient increase in EBV-specific CD8+ T cells in three patients; this may be due to a programmed proliferation of T cells.[10–12] In studies in mice, the decrease in pathogen-specific CD8+ T cells is programmed and independent of antigen loads (programmed contraction).[13,14] This is in agreement with current concepts of antigen-driven expansion and contraction of CD8+ T cells during acute infection.[3] A recent paper proposed the model of EBV dynamics in post-transplant lymphoproliferative disorders.[15] The model estimates both doubling times and half-lives of EBV in various situations under the antiviral agents, Rituximab, or adoptive immunotherapy with or without taking into account episomal or lytic origins.

In conclusion, the shorter half-life of EBV load together with the strong correlation between EBV-specific CD8+ T cell numbers and the rate of change of viral load suggests an active role for EBV-specific CD8+ T cells in the elimination of EBV. Further investigations of the interaction between EBV and EBV-specific CD8+ T cells during the period of increasing viral load will be necessary to understand the dynamic interaction between EBV and the immune system during AIM.

Conflict of interest statement

All authors state that they have no conflicts of interest that could inappropriately influence this work.

Acknowledgements

We thank Drs. Jeffrey I. Cohen and Kennichi C. Dowdell at Laboratory of Clinical Infectious Diseases, NIAID, for advice and suggestions. This study was supported by a grant from the Ministry of Education, Culture, Sports, Science and Technology of Japan (13670793).

References

1. Cohen JI. Epstein-Barr virus infection. *N Engl J Med* 2000;**343**(7):481–92.
2. Hislop AD, Taylor GS, Sauce D, Rickinson AB. Cellular responses to viral infection in humans: lessons from Epstein-Barr virus. *Annu Rev Immunol* 2007;**25**:587–617.
3. Hoshino Y, Morishima T, Kimura H, Nishikawa K, Tsurumi T, Kuzushima K. Antigen-driven expansion and contraction of CD8+-activated T cells in primary EBV infection. *J Immunol* 1999;**163**(10):5735–40.
4. Kimura H, Morita M, Yabuta Y, Kuzushima K, Kato K, Kojima S, et al. Quantitative analysis of Epstein-Barr virus load by using a real-time PCR assay. *J Clin Microbiol* 1999;**37**(1):132–6.
5. Hoshino Y, Kimura H, Tanaka N, Tsuge I, Kudo K, Horibe K, et al. Prospective monitoring of the Epstein-Barr virus DNA by a real-time quantitative polymerase chain reaction after allogenic stem cell transplantation. *Br J Haematol* 2001;**115**(1):105–11.
6. Kuzushima K, Kimura H, Hoshino Y, Yoshimi A, Tsuge I, Horibe K, et al. Longitudinal dynamics of Epstein-Barr virus-specific cytotoxic T lymphocytes during posttransplant lymphoproliferative disorder. *J Infect Dis* 2000;**182**(3):937–40.
7. Macallan DC, Wallace DL, Zhang Y, Ghattas H, Asquith B, de Lara C, et al. B-cell kinetics in humans: rapid turnover of peripheral blood memory cells. *Blood* 2005;**105**(9):3633–40.
8. Hochberg D, Souza T, Catalina M, Sullivan JL, Luzuriaga K, Thorley-Lawson DA. Acute infection with Epstein-Barr virus targets and overwhelms the peripheral memory B-cell compartment with resting: latently infected cells. *J Virol* 2004;**78**(10):5194–204.
9. Hadinoto V, Shapiro M, Greenough TC, Sullivan JL, Luzuriaga K, Thorley-Lawson DA. On the dynamics of acute EBV infection and the pathogenesis of infectious mononucleosis. *Blood* 2008;**111**(3):1420–7.
10. Kaech SM, Ahmed R. Memory CD8+ T cell differentiation: initial antigen encounter triggers a developmental program in naive cells. *Nat Immunol* 2001;**2**(5):415–22.
11. van Stipdonk MJ, Lemmens EE, Schoenberger SP. Naive CTLs require a single brief period of antigenic stimulation for clonal expansion and differentiation. *Nat Immunol* 2001;**2**(5):423–9.
12. van Stipdonk MJ, Hardenberg G, Bijker MS, Lemmens EE, Droin NM, Green DR, et al. Dynamic programming of CD8+ T lymphocyte responses. *Nat Immunol* 2003;**4**(4):361–5.
13. Badovinac VP, Porter BB, Harty JT. Programmed contraction of CD8(+) T cells after infection. *Nat Immunol* 2002;**3**(7):619–26.
14. Badovinac VP, Harty JT. Programming, demarcating, and manipulating CD8+ T-cell memory. *Immunol Rev* 2006;**211**:67–80.
15. Funk GA, Gosert R, Hirsch HH. Viral dynamics in transplant patients: implications for disease. *Lancet Infect Dis* 2007;**7**(7):460–72.

UICC
global cancer control

International Journal of Cancer

Bortezomib induces apoptosis in T lymphoma cells and natural killer lymphoma cells independent of Epstein-Barr virus infection

Seiko Iwata[1], Shoko Yano[1], Yoshinori Ito[2], Yoko Ushijima[1], Kensei Gotoh[2], Jun-ichi Kawada[3], Shigeyoshi Fujiwara[4], Koichi Sugimoto[5], Yasushi Isobe[5], Yukihiro Nishiyama[1] and Hiroshi Kimura[1]

[1] Department of Virology, Nagoya University Graduate School of Medicine, Nagoya, Japan
Department of Pediatrics, Nagoya University Graduate School of Medicine, Nagoya, Japan
[3] Department of Infection and Immunology, Aichi Children's Health and Medical Center, Aichi, Japan
[4] Department of Infectious Diseases, National Research Institute for Child Health and Development, Tokyo, Japan
[5] Department of Hematology, Juntendo University School of Medicine, Tokyo, Japan

Epstein-Barr virus (EBV), which infects not only B cells, but also T cells and natural killer (NK) cells, is associated with multiple lymphoid malignancies. Recently, the proteasome inhibitor bortezomib was reported to induce apoptosis of EBV-transformed B cells. We evaluated the killing effect of this proteasome inhibitor on EBV-associated T lymphoma cells and NK lymphoma cells. First, we found that bortezomib treatment decreased the viability of multiple T and NK cell lines. No significant difference was observed between EBV-positive and EBV-negative cell lines. The decreased viability in response to bortezomib treatment was abrogated by a pan-caspase inhibitor. The induction of apoptosis was confirmed by flow cytometric assessment of annexin V staining. Additionally, cleavage of caspases and polyadenosine diphosphate-ribose polymerase, increased expression of phosphorylated IκB, and decreased expression of inhibitor of apoptotic proteins were detected by immunoblotting in bortezomib-treated cell lines. We found that bortezomib induced lytic infection in EBV-positive T cell lines, although the existence of EBV did not modulate the killing effect of bortezomib. Finally, we administered bortezomib to peripheral blood mononuclear cells from five patients with EBV-associated lymphoproliferative diseases. Bortezomib had a greater killing effect on EBV-infected cells. These results indicate that bortezomib killed T or NK lymphoma cells by inducing apoptosis, regardless of the presence or absence of EBV.

Key words: Epstein-Barr virus, proteasome inhibitor, apoptosis, lytic infection, NF-κB

Abbreviations: 7-AAD: 7-aminoactinomycin D; BARTs: *Bam*HI-A rightward transcripts; cIAP: cellular IAP; DMSO: dimethyl sulfoxide; EBV: Epstein-Barr virus; EBER: EBV-encoded small RNA; EBNA: EBV nuclear antigen; FISH: Flow cytometric in situ hybridization; IAPs: inhibitors of apoptotic proteins; LMP: latent membrane protein; LCL: lymphoblastoid cell line; MNCs: mononuclear cells; NK: natural killer; NF-κB: nuclear factor-κB; PBS: phosphate-buffered saline; PE: phycoerythrin; PARP: polyadenosine diphosphate-ribose polymerase; RT: reverse transcription; SDS: sodium dodecyl sulfate; XIAP: X-linked IAP; β2m: β2-microglobulin

Grant sponsor: Ministry of Education, Culture, Sports, Science and Technology, Japan; **Grant number:** H21-Nanchi-094; **Grant sponsor:** Ministry of Health, Labor, and Welfare of Japan (Health and Labour Science Research Grant on intractable diseases)
DOI: 10.1002/ijc.25873
History: Received 17 Jun 2010; Accepted 30 Nov 2010; Online 17 Dec 2010

Correspondence to: Hiroshi Kimura, Department of Virology, Nagoya University Graduate School of Medicine, 65 Tsurumai-cho, Showa-ku, Nagoya 466-8550, Japan, Tel.: +81-52-744-2451
Fax: +81-52-744-2452, E-mail: hkimura@med.nagoya-u.ac.jp

The ubiquitous Epstein-Barr virus (EBV) infects most individuals by early adulthood and typically remains latent throughout life. EBV not only infects B cells but also T cells and natural killer (NK) cells and has been associated with multiple lymphoid malignancies such as Burkitt lymphoma, diffuse large B cell lymphoma, Hodgkin lymphoma, post-transplant lymphoproliferative disorders, nasal NK/T lymphoma, hydroa vacciniforme-like lymphoma, aggressive NK cell leukemia, and chronic active EBV infection.[1–4] EBV plays an important role in the pathogenesis of many of these malignancies through its ability to establish latent infection and induce the proliferation of infected cells.[5] Some of these EBV-associated lymphoid malignancies are refractory and resistant to conventional chemotherapies. Rituximab, a humanized monoclonal antibody against CD20, targets B cell-specific surface antigens present on EBV-transformed malignant cells. Currently, Rituximab is used in the treatment and prophylaxis of B cell lymphoma and lymphoproliferative disorders.[6,7] However, a continuing need exists for effective treatments of T and NK cell lymphoid malignancies, and novel approaches of molecular target therapy are desirable.

Recently, bortezomib was reported to induce apoptosis in EBV-transformed B cells and prolong survival of mice inoculated with EBV-transformed B cells.[8] Bortezomib is an inhibitor of the 26S proteasome.[9] Proteasomes are multi-protein

complexes that degrade ubiquitinated proteins, including those involved in cell cycle regulation, oncogenesis, and apoptosis. Inhibition of the proteasome can result in apoptosis in malignant cells.[10,11] Bortezomib is approved for the treatment of multiple myeloma and is in clinical trials for non-Hodgkin lymphoma, prostate cancer, and lung cancer.[12,13] A key factor in the ability of bortezomib to kill myeloma cells is that it blocks the activation of nuclear factor-κB (NF-κB).[14] In normal cells, NF-κB is bound to the inhibitory protein IκB, which maintains it in an inactive form in the cytoplasm. Once activated, NF-κB can then enter the nucleus and initiate many actions in the tumor cell that help the cell to survive and proliferate. As a result of inhibiting the proteasome and thus the activation of NF-κB, bortezomib may induce apoptosis by reducing the expression of inflammatory molecules and cell adhesion molecules.[14] Additionally, a study has reported that bortezomib can lead to EBV lytic infection.[15] In EBV-infected lymphocytes, only a few viral genes are expressed to maintain latency and to avoid host immune mechanisms.[1,5] Bortezomib may alter the pattern of viral gene expression thus converting a latent infection to a lytic infection.

In our study, we evaluated the killing effect of bortezomib on EBV-associated T/NK lymphoma cells. To investigate the mechanism of killing, we administered bortezomib to multiple EBV-positive and -negative T and NK cell lines. We further administered bortezomib *ex vivo* to lymphoma cells from patients with EBV-associated lymphoid malignancies.

Material and Methods

Cell lines and reagents

Raji, a latency type III cell line, is an EBV-positive B cell line derived from Burkitt lymphoma.[16] Lymphoblastoid cell line (LCL)-1 and LCL-2, latency type III cell lines, are EBV-positive B cell lines transformed with B95-8 EBV from peripheral blood B lymphocytes. BJAB is an EBV-negative B cell line. SNT-13 and SNT-16[17] are EBV-positive T cell lines. SNK-6[17] and KAI-3[18] are EBV-positive NK cell lines. SNT-13, -16, SNK-6, and KAI-3 were derived from patients with chronic active EBV infection or nasal NK/T cell lymphomas. Jurkat[19] and KHYG-1[20] are EBV-negative T and NK cell lines, respectively. Jurkat was derived from a patient with acute T lymphoblastic leukemia. KHYG-1 was derived from a patient with aggressive NK cell leukemia.

MT-2 cell line was established from cord mononuclear cells by co-culture with adult T cell leukemia cells, and harbors human T cell-leukemia virus type I.[21] MT-2/rEBV/9-7 cell line was established by infection of MT-2 cells with the hygromycin-resistant B95-8 strain.[22] MT-2/hyg cell line, transfected with a hygromycin-resistant gene, and MT-2/rEBV/9-7 were used to verify the difference of EBV presence in the T cell lines. Similarly, NKL cell line[23] was derived from a patient with NK cell leukemia, and TL1 cell line[24] was established from NKL cells infected with Akata-transfected recombinant EBV strain containing a neomycin-resistant gene. TL1 and NKL were used to verify the difference of EBV presence in the NK cell lines.

Raji, LCL-1, LCL-2, BJAB, and Jurkat cells were grown in RPMI 1640 supplemented with 10% heat-inactivated fetal bovine serum, penicillin, and streptomycin (complete media). The medium for SNT-13, -16, KAI3, SNK-6, KHYG1, TL1, and NKL was complete media supplemented with 100 U/ml human interleukin-2. The medium for MT-2/hyg and MT-2/rEBV/9-7 was complete media supplemented with 0.2 mg/ml hygromycin. TL1 underwent periodic selection with G418.

Bortezomib, a gift from Millennium Pharmaceuticals (Cambridge, MA), was dissolved in phosphate-buffered saline (PBS). The pan-caspase inhibitor Q-VD-OPH (Calbiochem, La Jolla, CA) and the proteasome inhibitor MG132 (Biomol International, Plymouth Meeting, PA) were dissolved in dimethyl sulfoxide (DMSO).

Cell viability and apoptosis assays

Cells (2×10^5/ml) were cultured in 24-well plates and cell viability was quantified by trypan blue exclusion. The pan-caspase inhibitor Q-VD-OPH (50 μM) was added at 1 hr prior to the addition of bortezomib. These experiments were performed in duplicate and the results are shown as the mean of two wells.

Apoptosis was measured by flow cytometry using an annexin V-phycoerythrin (PE)/7-aminoactinomycin D (7-AAD) apoptosis assay kit (BD Pharmingen Biosciences, San Diego, CA) according to the manufacturer's protocol. Briefly, 2×10^5 cells were treated with various concentrations of bortezomib for 6 hr, washed with ice-cold PBS, resuspended in binding buffer, incubated with annexin V-PE and 7-AAD for 15 min, and then analyzed by flow cytometry. Viable cells were defined as those negative for annexin V-PE and 7-AAD staining, and early apoptotic cells were defined as those positive for annexin V-PE and negative for 7-AAD staining. Stained cells were analyzed using a FACSCalibur and CellQuest software (Becton Dickinson, Franklin Lakes, NJ).

Immunoblots

Whole-cell extracts were lysed directly with sodium dodecyl sulfate (SDS) sample buffer (50 mM Tris-HCl, pH 6.8, 2% SDS, 10% glycerol, 6% 2-mercaptoethanol, 0.0025% bromophenol blue). Cell lysates were separated by SDS-polyacrylamide gel electrophoresis and transferred to polyvinylidene difluoride membranes (Immobilon-P membrane; Millipore), and immunoblotted with antibodies. Antibodies were directed against caspase-3, cleaved caspase-3, caspase-9, phosphorylated IκBα, and polyadenosine diphosphate-ribose polymerase (PARP) (Cell Signaling Technology, Beverly, MA); β-actin (Sigma, St. Louis, MO); XIAP and cIAP-2 (R&D Systems, Minneapolis, MN); and p53 (BD Pharmingen Biosciences). To compare the amounts of each protein, densitometoric analysis was performed using ImageJ software ver. 1.43 (NIH, Bethesda, MD).

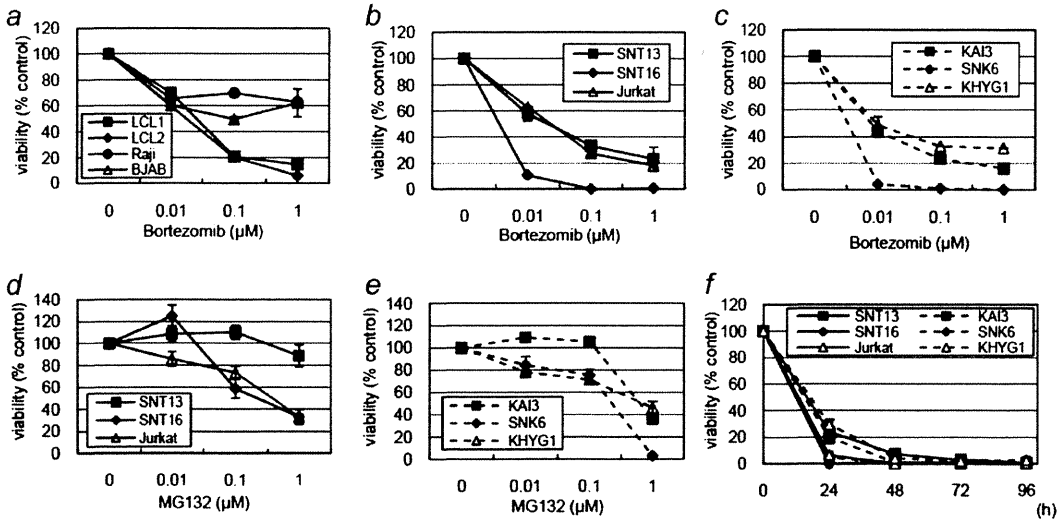

Figure 1. Bortezomib decreases the viability of B, T and NK cell lines. (*a*) B cell lines (Raji, LCL-1, LCL-2, BJAB), (*b*) T cell lines (SNT-13, SNT-16, Jurkat), and (*c*) NK cell lines (KAI-3, SNK-6, KHYG-1) were treated with bortezomib at the indicated concentrations for 24 hr. (*d*) T cell lines or (*e*) NK cell lines were treated with MG132 at various concentrations for 24 hr. (*f*) T or NK cell lines were treated with 1 μM bortezomib for 4 days and viability was determined every 24 hr. The filled markers represent EBV-positive cell lines and the open markers represent EBV-negative cell lines. Viability was calculated as the percentage of viable cells in bortezomib-treated cells *versus* PBS-treated cells. Bars indicate standard errors.

Real-time RT-PCR assay

RNA was extracted from 1×10^6 cells using the QIAmp RNeasy Mini Kit (Qiagen, Hilden, Germany). Contaminating DNA was removed by on-column deoxyribonuclease digestion using the RNase-Free DNase Set (Qiagen). Viral mRNA expression was quantified by a one-step multiplex real-time reverse transcription (RT)-PCR using a Mx3000P real-time PCR system (Stratagene, La Jolla, CA), as described previously.[25,26] The stably expressed housekeeping gene β2-microglobulin (β2m) was used as an endogenous control and reference gene for relative quantification.[27] Each experiment was conducted in triplicate and results are shown as the mean of three samples with standard errors. The Mann-Whitney *U*-test was used to compare the expression levels. p values <0.05 were deemed to be statistically significant.

Patients

Peripheral blood mononuclear cells (MNCs) were collected from five patients with EBV-associated diseases. None of these patients had received any immunosuppressive treatment such as steroid therapy or chemotherapy. Patients T-1 (7-year-old boy), T-2 (6-year-old girl), and T-3 (12-year-old boy) had hydroa vacciniforme-like lymphoma, a newly classified EBV-associated T cell lymphoma.[2] In these patients, 10~20% of the MNCs were infected with EBV, and the EBV-infected cells were primarily γδT cells.[28] The other two patients, Patients NK-1 (14-year-old boy) and NK-2 (9-year-old boy), had chronic active EBV infection, NK cell type.[29–31] In these patients, ~40% of MNCs were infected with EBV, and the EBV-infected cells were NK cells. MNCs from three healthy donors were used as controls. Informed consent was obtained from all participants or their guardians. Our study was approved by the institutional review board of Nagoya University Hospital.

MNCs were isolated using Ficoll-Paque (Amersham Pharmacia Biotech AB, Uppsala, Sweden) gradient centrifugation. Cells (2×10^5/ml) were cultured in RPMI 1640 supplemented with 10% heat-inactivated fetal bovine serum. For the cell viability study, each experiment was performed in duplicate, and the results are shown as the mean of two wells.

Magnetic cell sorting

The primarily infected cell fractions were separated by magnetic sorting with a TCRγ/δ$^+$ T Cell Isolation Kit or CD56 Microbeads (Miltenyi Biotec, Bergisch Gladbach, Germany). Briefly, cells were magnetically labeled with MicroBeads and separated on a column placed in the MACS separator. The flow-through was collected as a negative fraction depleted of the labeled cells. The magnetically retained cells were flushed out as the positive fraction. The respective purity and recovery rates were 98.3% and 80.0% with the TCRγ/δ$^+$ T Cell Isolation Kit, and 96.4% and 80.9% with CD56 Microbeads.

Flow cytometric in situ hybridization (FISH) assay

To verify that the sorted fraction contained EBV-infected cells, a FISH assay was used.[28] Briefly, cells were fixed with 1% acetic acid/4% paraformaldehyde, permeabilized with 0.5% Tween 20/PBS, and hybridized with a fluorescein-labeled

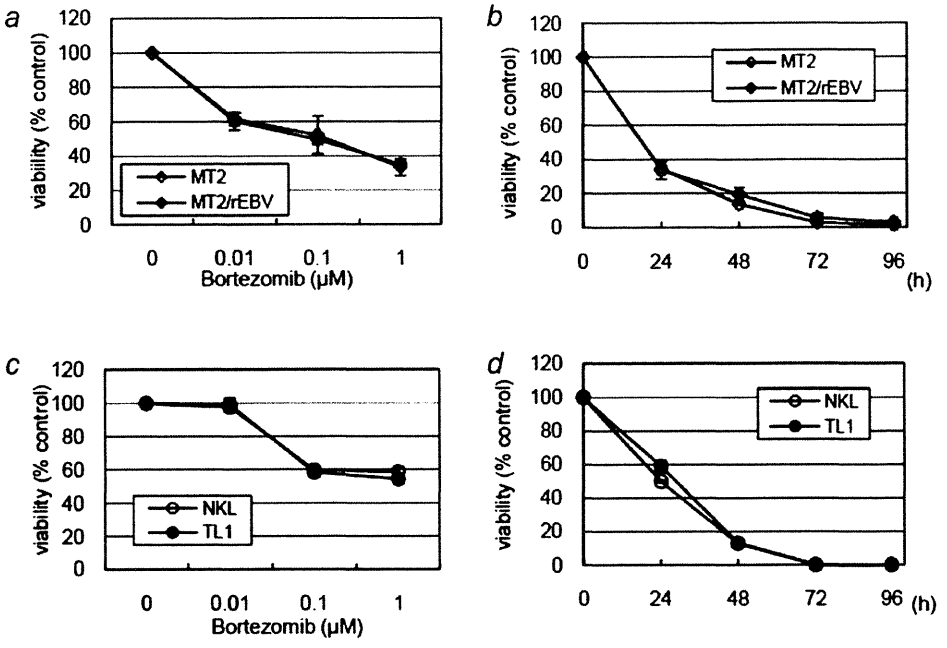

Figure 2. Bortezomib induces similar effects in EBV-positive and -negative cell lines. An EBV-positive T cell line (MT-2/rEBV) and a control cell line (MT/hyg) were treated with various concentrations of bortezomib for 24 hr (*a*) and 1 μM bortezomib for 4 days (*b*). EBV-positive NK cell line (TL1) and its parental line (NKL) were treated with various concentrations of bortezomib for 24 hr (*c*) and 1 μM bortezomib for 4 days (*d*). Bars indicate standard errors.

EBV-encoded small RNA (EBER)-specific peptide nucleic acid probe (Y5200; Dako, Glostrup, Denmark). The fluorescence intensity was enhanced using the AlexaFluor 488 Signal Amplification Kit (Molecular Probes, Eugene, OR), and stained cells were analyzed using a FACSCalibur and CellQuest software (Becton Dickinson).

Results

Bortezomib decreased the viability of B, T and NK cell lines

First, we administered bortezomib to B, T and NK cell lines for 24 hr and counted viable cells. Bortezomib decreased the viability of all four B cell lines: three EBV-positive cell lines (Raji, LCL-1, and LCL-2) and one EBV-negative cell line (BJAB) (Fig. 1*a*). LCL-1 and LCL-2 were more sensitive to bortezomib than Raji or BJAB, consistent with the results of a previous study reporting that bortezomib killed both EBV-positive and -negative B cell lines, but more efficiently in LCLs.[8] Next, we administered bortezomib to T cell lines (SNT-13, SNT-16, Jurkat) and NK cell lines (KAI-3, SNK-6, KHYG-1). Bortezomib decreased the viability of all six target cell lines in a dose-dependent manner (Figs. 1*b* and 1*c*). SNT-16 and SNK-6 seemed to be more sensitive to bortezomib than other cell lines. MG132, another proteasome inhibitor, had less effect on these cell lines (Figs. 1*d* and 1*e*). We administered 1 μM bortezomib to these cell lines for 4 days and determined their viability every 24 hr. We found that bortezomib decreased the viability of these six cell lines by less than 10% at 48 hr or later (Fig. 1*f*). There were no obvious differences on the effect of bortezomib between the EBV-positive and -negative cell lines. Furthermore, to directly compare the effect of bortezomib between EBV-positive and -negative cell lines, we administered bortezomib to MT-2/hyg and MT-2/rEBV/9-7 (Figs. 2*a* and 2*b*), and NKL and TL1 (Figs. 2*c* and 2*d*). We found that bortezomib had almost equal effects on the two cell lines.

Bortezomib induces apoptosis in T and NK cell lines

The induction of apoptosis was confirmed by flow cytometry with annexin V and 7-AAD staining. Bortezomib decreased viable cells, defined as those negative for both annexin V-PE and 7-AAD staining, and increased early apoptotic cells, defined as those positive for annexin V-PE and negative for 7-AAD staining in the four cell lines (Fig. 3*a*): EBV-positive (SNT-16) and EBV-negative T cell lines (Jurkat); and EBV-positive (KAI-3) and EBV-negative NK cell lines (KHYG-1). This result showed that bortezomib induced apoptosis in both T and NK cell lines.

Next, to analyze the mechanism of bortezomib-induced apoptosis, cleavages of caspase and PARP were investigated by immunoblotting. Bortezomib induced cleavage of caspase-3, caspase-9, and PARP in all four cell lines (Fig. 3*b*). The decrease in viability caused by bortezomib was inhibited by pretreatment with Q-VD-OPH, a pan-caspase inhibitor (Fig. 3*c*).

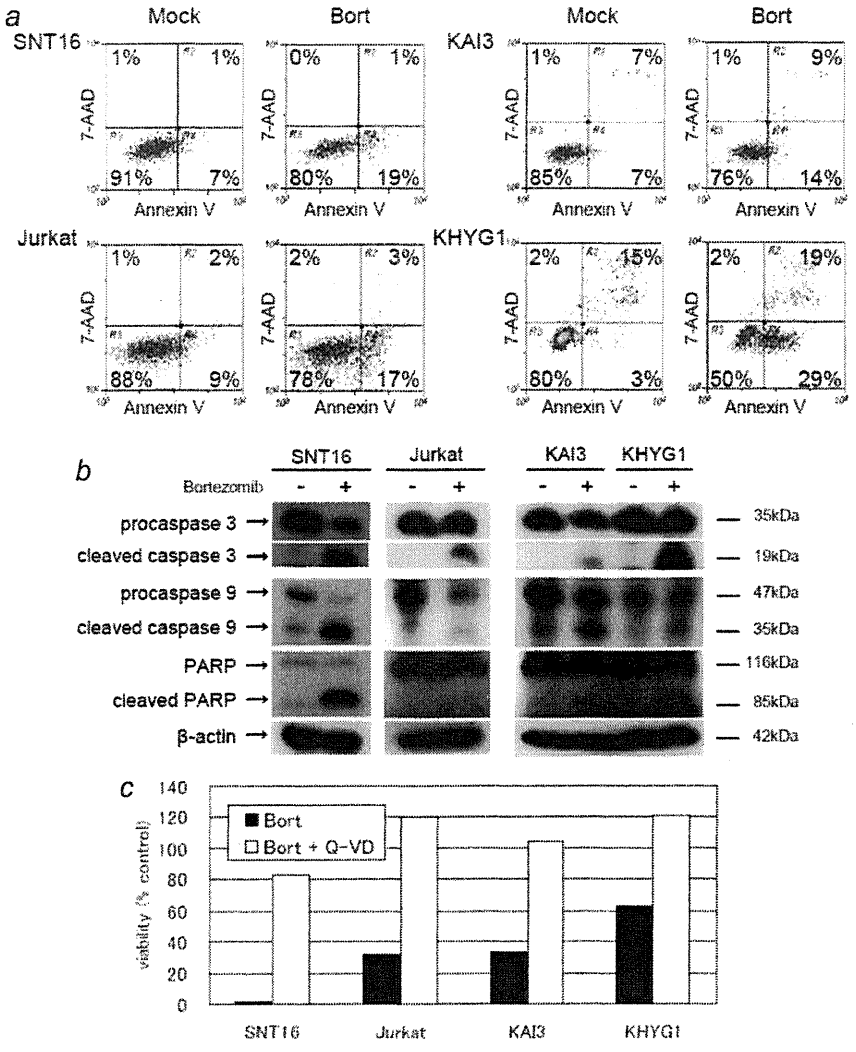

Figure 3. Bortezomib induces apoptosis in T/NK cell lines. (*a*) T cell lines (EBV-positive SNT-16 and -negative Jurkat) and NK cell lines (EBV-positive KAI-3 and -negative KHYG-1) were treated with 1 μM bortezomib for 6 hr. Viable cells were defined as those negative for annexin V-PE and 7-AAD staining, and early apoptotic cells were defined as those positive for annexin V-PE and negative for 7-AAD staining. (*b*) Bortezomib induces cleavage of caspase-3, caspase-9, and PARP. T/NK cell lines were treated with 1 μM bortezomib for 6 hr. Protein lysates were prepared and immunoblotting was performed. β-actin was used as a loading control. Each experiment was performed at least twice. (*c*) Q-VD-OPH inhibits the decrease in viability induced by bortezomib. The pan-caspase inhibitor Q-VD-OPH (50 μM) was added 1 hr prior to the addition of 1 μM bortezomib for 24 hr. Viability was calculated as the percentage of viable cells to PBS-treated cells as assessed by trypan blue exclusion.

Bortezomib blocks activation of NF-κB by inhibiting the proteasome, reducing antiapoptotic factors

In myeloma cells, bortezomib blocks the activation of NF-κB through increasing phosphorylation of IκB.[14] Thus, we confirmed the increase in phosphorylated IκB, which should have been degraded in proteasomes, in bortezomib-treated cell lines by immunoblotting (Fig. 4*a*). Furthermore, we evaluated the effect of bortezomib on two inhibitors of apoptotic proteins (IAPs). Bortezomib down-regulated cellular IAP (cIAP)-2 and X-linked IAP (XIAP) in bortezomib-treated T/NK cell lines (Fig. 4*b*). Densitometoric analysis was performed to confirm that cIAP-2 and XIAP were decreased in all bortezomib-treated cells (Fig. 4*c*). Additionally, bortezomib up-regulated p53, facilitating apoptosis, in some cell lines (Fig. 4*b*).

Bortezomib induces lytic infection of EBV in T cell lines

Next, we analyzed the expression of eight viral genes using a real-time RT-PCR assay: two lytic genes, BZLF1 and gp350/

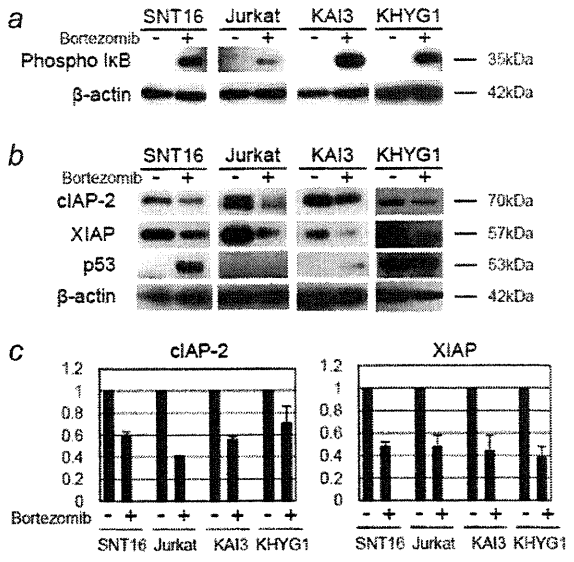

Figure 4. Bortezomib increases phosphorylated IκB and down-regulates the inhibitor of apoptotic proteins in T/NK cell lines. T cell lines (EBV-positive SNT-16 and -negative Jurkat) and NK cell lines (EBV-positive KAI-3 and -negative KHYG-1) were treated with 1 μM bortezomib for 2 hr (*a*) or 8 hr (*b*). Protein lysates were prepared and immunoblotting was performed. β-actin was used as a loading control. Each experiment was performed at least twice. (*c*) Densitometoric analysis was performed using ImageJ software. The data were calculated as the ratios of cIAP-2 (left) and XIAP (right) to β-actin, and the value of PBS-treated cells was assigned as 1. Boxes indicate the mean of two experiments and bars indicate the standard errors.

220; and six latent genes, EBV nuclear antigen (EBNA) 1, EBNA2, latent membrane protein (LMP) 1, LMP2, EBER1, and *Bam*HI-A rightward transcripts (BARTs). We found that the expression of two lytic genes, an immediate early gene (BZLF1) and a late gene (gp350/220), were increased in bortezomib-treated T cell lines (SNT-13 and SNT-16 in Fig. 5). In NK cell lines, however, no such effect was observed. Regarding latent genes, expression of LMP2 was increased in T cell lines. The expressions of other latent genes (EBNA1, EBNA2, LMP1, EBER1, and BARTs) were not obviously different between bortezomib-treated cells and controls (Fig. 5).

Bortezomib decreases the viability of EBV-infected cells from patients with EBV-associated lymphoma

Finally, we investigated the *ex vivo* effect of bortezomib in MNCs from five patients with EBV-associated malignancies. We separated γδT cells and other MNCs from three patients (Patients T-1, T-2, and T-3) with hydroa vacciniforme-like lymphoma by magnetic sorting. Bortezomib (0.5 μM) was administered to each sample of cells, and the viable cells were counted for 3 days. Bortezomib had a greater killing effect on γδT cells that were primarily infected with EBV than on the other MNCs (Fig. 6*a*). Next, we separated the NK cells and other MNCs from two patients (Patients NK-1, and NK-2) with chronic active EBV infection, NK cell-type, and evaluated the effect of bortezomib. For Patient NK-1, experiments were performed twice on different visits. Bortezomib had a greater killing effect on NK cells than on the other MNCs (Fig. 6*b*). In the γδT cell or NK-cell fraction, the absolute number of control viable cells was stable or increased slightly, while the number was clearly decreased with bortezomib treatment (data not shown). Next, we collected blood samples from three healthy donors, sorted the γδT cells, NK cells, and other MNCs, and evaluated their viability with bortezomib treatment. The viability of the cells treated with bortezomib for 3 days was around 100%, indicating that bortezomib did not affect nontumor cells (Fig. 6*c*).

To confirm that the sorted fractions contained EBV-infected cells, EBER-positive cells were quantified using a FISH assay. In Patient T-1 with hydroa vacciniforme-like lymphoma, 19.8% of the MNCs were EBER-positive. After magnetic sorting, 54.7% of γδT cells and 3.8% of the other MNCs were EBER-positive (Fig. 6*d*). To determine whether EBV-infected cells survive selectively, we quantified EBV-positive cells using the FISH assay after bortezomib treatment, and compared the results with PBS-treated control cells. After 3 days, the percentage of EBER-positive bortezomib-treated γδT cells decreased (4.0%), as compared to PBS-treated γδT cells (47.8%) (Fig. 6*e*). Similarly, the percentage of EBER-positive cells in bortezomib-treated NK cells decreased (0.5%), as compared to PBS-treated NK cells (34.1%) (Fig. 6*e*). These results indicate that EBV-positive cells in the control groups survived, while most EBV-positive bortezomib-treated γδT and NK cells died. Moreover, this killing effect was confirmed by flow cytometry using annexin V and 7-AAD staining in Patient NK-1 (Fig. 6*f*).

Discussion

Bortezomib, which is used in the treatment of myeloma, has also been assessed for a variety of other malignancies. In recent studies, this proteasome inhibitor was reported to induce apoptosis in NK lymphoma/leukemia cells,[32,33] and has been tested in cutaneous T cell lymphomas and aggressive T/NK cell lymphomas, including EBV-associated ones.[34,35] Although promising data have accumulated, these trials were small and must be considered preliminary. Furthermore, experience with EBV-associated cases is limited. To our knowledge, there have been no *in vitro* studies to compare the efficacy of bortezomib between EBV-positive and EBV-negative T/NK lymphoma cells.

In our study, we treated T and NK cell lines with bortezomib to investigate this proteasome inhibitor's ability to induce apoptosis in T and NK lymphoma cells. Bortezomib markedly decreased the viability of T and NK cell lines by inducing apoptosis. Consistent with previous reports, the cleavage of caspases and PARP, increased phosphorylated IκB, and the decreased inhibitor apoptotic proteins indicated

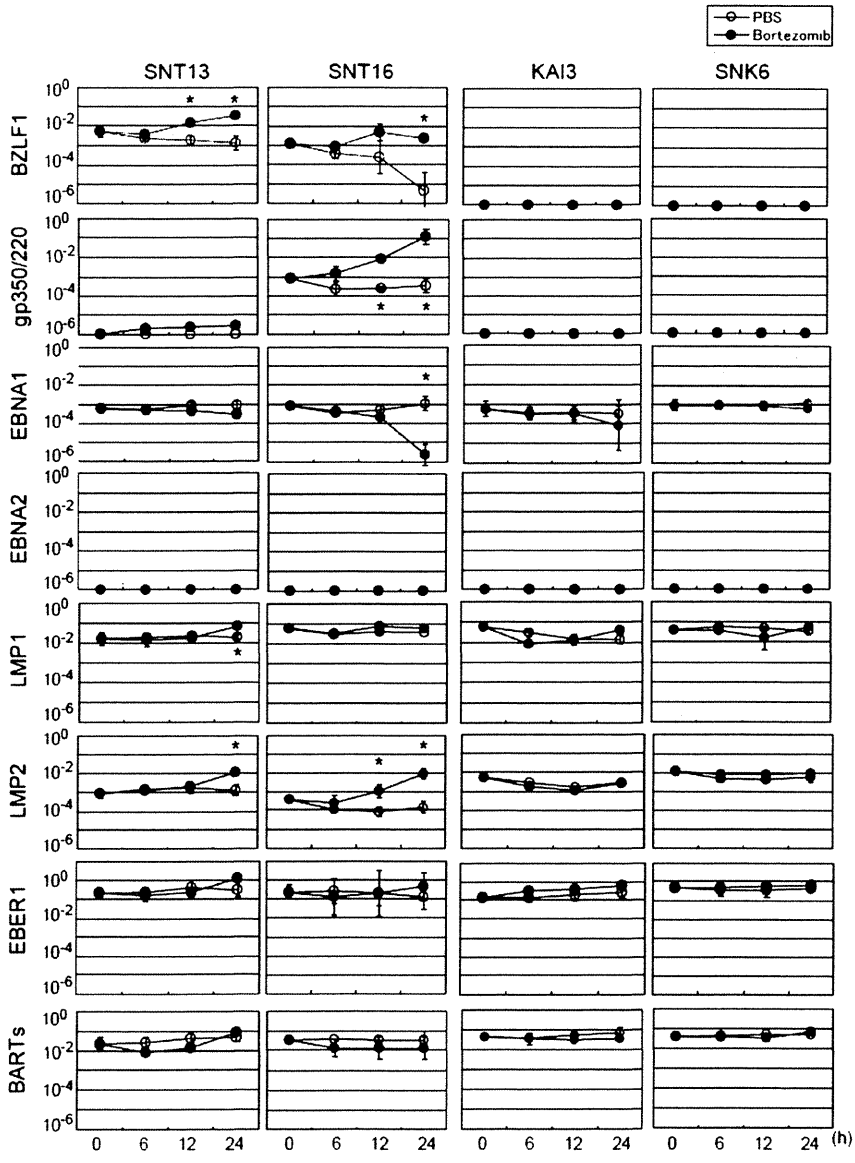

Figure 5. Bortezomib induces lytic infection of EBV in T cell lines. EBV-positive T cell lines (SNT-13 and SNT-16) and EBV-positive NK cell lines (KAI-3 and SNK-6) were treated with 1 μM bortezomib and collected at 0, 6, 12, and 24 hr to evaluate the expression of EBV-encoded genes by real-time RT-PCR. BZLF1 is an immediate early gene and gp350/220 is a late gene. EBNA1, EBNA2, LMP1, LMP2, EBER1, and BARTs are latent genes. β2-microglobulin was used as an endogenous control and reference gene for relative quantification and assigned an arbitrary value of 1 (10^0). Closed circles indicate bortezomib-treated cells, while open circles denote PBS-treated cells. Bars indicate standard errors. *$p < 0.05$ by Mann-Whitney *U*-test.

that this apoptosis was due to bortezomib inhibiting the degradation of phosphorylated IκB.[8,14,36] The inhibition of phosphorylated IκB degradation restrains the activation of NF-κB, which is associated with chemoresistance and poor survival in T and NK cell lymphomas.[37,38] We found, however, no significant difference between EBV-positive and -negative cell lines. The findings suggest that the mechanism of bortezomib in eliminating malignant cells involves the inhibition of NF-κB activation inducing apoptosis and preventing the immortalization and proliferation of cells. Other mechanisms by which bortezomib acts against malignancies, such as the stabilization of p53, disruption of the cell cycle, induction of endoplasmic reticulum stress, and increased intracellular reactive oxygen species, have been reported.[39,40]